GCM Simulations of Volcanic Aerosol Forcing. Part I: Climate Changes Induced by Steady-State Perturbations

JAMES B. POLLACK

Space Science Division, NASA/Ames Research Center, Moffett Field, California

DAVID RIND, ANDREW LACIS, JAMES E. HANSEN, MAKIKO SATO, AND RETO RUEDY

NASA/Goddard Space Flight Center, Institute for Space Studies, New York, New York

(Manuscript received 9 April 1991, in final form 16 January 1993)

ABSTRACT

The authors have used the Goddard Institute for Space Studies Climate Model II to simulate the response of the climate system to a spatially and temporally constant forcing by volcanic aerosols having an optical depth of 0.15. The climatic changes produced by long-term volcanic aerosol forcing are obtained by differencing this simulation and one made for the present climate with no volcanic aerosol forcing. These climatic changes are compared with those obtained with the same climate model when the CO_2 content of the atmosphere was doubled ($2\times CO_2$) and when the boundary conditions associated with the peak of the last ice age were used (18 K). In all three cases, the absolute magnitude of the change in the globally averaged air temperature at the surface is approximately the same, ~5 K.

The simulations imply that a significant cooling of the troposphere and surface can occur at times of closely spaced, multiple, sulfur-rich volcanic explosions that span time scales of decades to centuries, such as occurred at the end of the nineteenth and beginning of the twentieth centuries. The steady-state climate response to volcanic forcing includes a large expansion of sea ice, especially in the Southern Hemisphere; a resultant large increase in surface and planetary albedo at high latitudes; and sizable changes in the annually and zonally averaged air temperature, ΔT; ΔT at the surface (ΔT_s) does *not* sharply increase with increasing latitude, while ΔT in the lower stratosphere is positive at low latitudes and negative at high latitudes.

In certain ways, the climate response to the three different forcings is similar. Direct radiative forcing accounts for 30% and 25% of the total ΔT_s in the volcano and $2\times CO_2$ runs, respectively. Changes in atmospheric water vapor act as the most important feedback, and are positive in all three cases. Albedo feedback is a significant, positive feedback at high latitudes in all three simulations, although the land ice feedback is prominent only in the 18 K run.

In other ways, the climate response to the three forcings is quite different. The latitudinal profiles of ΔT_s for the three runs differ considerably, reflecting significant variations in the latitudinal profiles of the primary radiative forcing. Partially as a result of this difference in the ΔT_s profiles, changes in eddy kinetic energy, heat transport by atmospheric eddies, and total atmospheric heat transport are quite different in the three cases. In fact, atmospheric heat transport acts as a positive feedback at high latitudes in the volcano run and as a negative feedback in the other two runs. These results raise questions about the ease with which atmospheric heat transport can be parameterized in a simple way in energy balance climate models.

1. Introduction

Energetic volcanic explosions, such as those of Mount Agung, El Chichón, and Mount Pinatubo inject micron-sized silicate particles and gases, including sulfur-containing ones, into the stratosphere, where this material and its products have residence times of weeks to years. The silicates sediment out of the stratosphere on the shorter of these time scales, while sulfuric acid particles, produced by photochemical reactions involving the injected sulfur gases, persist for several years (Toon and Pollack 1982). Almost all of the impact of volcanic aerosols on the earth's radiation budget is produced by the longer-lived sulfuric acid aerosols (Pollack et al. 1976a; Toon and Pollack 1982; Pollack et al. 1983).

Sulfuric acid particles in the stratosphere affect climate by altering solar and terrestrial radiative fluxes. In particular, by absorbing warm upwelling thermal radiation from the surface and troposphere and reemitting thermal radiation at a much lower temperature, they warm the lower portion of the stratosphere within which they reside. The one-dimensional, radiative–convective calculations of Pollack and Ackerman (1983), which used data for the well-observed El Chi-

Corresponding author address: Dr. James B. Pollack, Space Science Division, NASA/Ames Research Center, Moffett Field, CA 94035.

chón volcanic cloud, reproduced well the stratospheric temperature increases associated with this cloud (Labitzke et al. 1983). These particles tend to cool the troposphere and surface by reducing the amount of sunlight reaching the troposphere and ground, and they tend to warm these regions by increasing the downward-directed thermal radiation at the tropopause (Pollack et al. 1976a). Simulations of temperature changes within the troposphere associated with the Agung eruption (Hansen et al. 1980) and evaluations of the radiative properties of the El Chichón particles (Pollack et al. 1991) indicate that the solar perturbation is stronger than the thermal perturbation; hence, volcanic aerosols generally produce a cooling of the atmosphere and surface below them. An obvious exception to this general rule is the impact of volcanic aerosols at high latitudes during the winter season, where their thermal effects should dominate (Harshvardhan et al. 1984).

Volcanic aerosols attained sufficiently high optical depths ($\sim$0.1) at times during the last 100 years to have contributed significantly to the climate forcing at these times (Pollack et al. 1976b; Hansen and Lacis 1990). In particular, the time-averaged optical depth of the stratospheric aerosols for the period from 1882 to 1914 was approximately 0.05 due to the culmulative effect of a number of major volcanic explosions during this period (Pollack et al. 1976b). Consequently, these particles, as well as a reduced level of greenhouse gases in the atmosphere at this time, may have contributed to a lower globally averaged surface temperature then than during much of the later epoch (Pollack et al. 1976b; Hansen and Lacis 1990).

We have used a general circulation model (GCM) to simulate the response of the climate system to a temporally and spatially constant amount of volcanic particles. The optical depth of these aerosols was chosen so as to produce approximately the same amount of forcing as results from doubling the present CO_2 content of the atmosphere and from the boundary conditions associated with the peak of the last ice age. This was done to abet comparisons with analagous experiments performed with the same GCM.

Our simulations have three major objectives. First, we wish to better understand the climate changes induced by volcanic particles. The current simulations are relevant to periods of several decades to centuries in which there was a sustained volcanic forcing engendered by multiple, closely spaced volcanic explosions, as has occurred in both historical times and earlier epochs (Pollack et al. 1976b; Toon and Pollack 1982). These simulations may also provide insight into the three-dimensional pattern of climate changes produced by a single volcanic cloud. These patterns are difficult to discern in both observations and calculations due to signal-to-noise limitations.

A second objective of our simulations is to assess the similarities and differences in the response of the climate system (aside from sign differences) to forcing by volcanoes, greenhouse gases, and ice age conditions. In particular, we are interested in determining the degree to which there is a "universal" response, as opposed to a forcing-dependent response, the degree to which forcings that cause coolings and warmings elicit the same response, aside from a sign change, in the climate system, and the degree to which forcings of the same sign yield the same response. To the degree that there are significant differences, one may have the ability to cleanly separate the response of the climate system to several concurrent forcings, a matter of considerable interest in view of the concern about the climatic impact of greenhouse gases over the next century.

The third objective of our simulations is to perform a limited assessment of parameterizations used in energy balance climate models. Such models commonly assume that there are simple relationships between transports by eddies and spatial gradients in the mean fields. By comparing the vigor of the eddy transports among the three GCM climate experiments and their relationship to mean fields, we will evaluate the appropriateness of some of the commonly used parameterizations.

2. Procedure

We performed the volcano simulations with the Goddard Institute for Space Studies (GISS) climate model II (Hansen et al. 1983; henceforth, paper 1). In this section, we first describe several key aspects of this climate model and then discuss the properties of the volcanic particles used in the volcano simulation. In describing the application of climate model II to the volcano problem, we will also indicate the manner in which this model was used in prior simulations of steady-state changes occurring when the present atmospheric CO_2 content was doubled ($2\times CO_2$) and when the surface had properties similar to that at the peak of the last ice age (18 K—^{14}C age) (Hansen et al. 1984; henceforth paper 2).

As is the case for all modern GCMs, the primitive equations of meteorology are numerically integrated to determine the temporal evolution of the basic atmospheric fields: temperature, pressure, wind, and moisture. In view of the quasi-chaotic nature of the nonlinear primitive equations, it is not possible to make totally deterministic predictions of the temporal evolution of the climate system for periods in excess of about a day from the initial time point. However, the response of the climate system is not totally random for a given forcing (e.g., doubling CO_2 always results in a global warming, regardless of the exact initial conditions). Thus, it should be possible to make statistically meaningful statements about the response of the climate system to a given forcing.

Since the GCM had to be run for 55 simulated years to reach a statistically steady state for the volcanic

problem of interest, we used a coarse grid of 8° latitude by 10° longitude. The dynamical portion of the model is divided into nine vertical layers that span the region from the surface to a pressure level of 10 mb. The two highest-lying levels are situated in the lower stratosphere, where the volcanic particles are located (these two layers span pressures ranging from 10 to 70 mb and 70 to 150 mb, respectively). In addition, there are three layers situated at still higher altitudes that influence the radiation fields in the lower-lying, dynamical portion of the model. The same grids were used in the $2\times$ CO_2 and the 18 K ice age experiments with which the volcano run will be compared. As discussed in detail in paper 1, many aspects of the current climate are well simulated with model II with its coarse horizontal resolution, although there are some deficiencies.

For the volcano problem, as well as for the $2\times$ CO_2 problem, sea surface temperature and sea ice cover are calculated, instead of being prescribed. Sea surface temperature was calculated from the first law of thermodynamics, in which fixed but nonzero oceanic heat transport and a seasonally and spatially variable depth for the mixed layer of the ocean were included. The oceanic heat transports were derived from model II simulations of the present climate regime, for which observed sea surface temperatures and sea ice distribution were used (paper 2). Relevant data were used to define the depth of the mixed layer (NOAA 1974; Gordon 1982).

Sea ice begins to form when the temperature of the mixed layer decreases to -1.6°C, the freezing point of seawater, with the fractional amount of ice cover in each grid box increasing as the ice thickness increases. A surface energy budget is used to determine the formation, thickness, fractional coverage, and dissipation of sea ice (paper 2).

In contrast to the volcano and $2\times$ CO_2 simulations, the 18 K ice age experiment was carried out with prescribed ocean temperatures, sea ice, continental snow, and continental topography that were based on the Climate: Long-Range Investigation, Mapping, and Prediction Project (CLIMAP) data (CLIMAP 1981; Denton and Hughes 1981). Thus, there is an ocean heat transport feedback in the 18 K experiment, since it can be independently determined for the 18 K experiment and its control run (the present climate) from the heat budget at the ocean surface.

For all three climate perturbation experiments, fractional cloud cover and cloud height were calculated, although the radiative properties of clouds at a fixed altitude level were held constant. Thus, cloud feedbacks are included in the simulations, although in a somewhat incomplete manner.

Results from all three experiments were compared with the properties of the "unperturbed" present climate, as simulated with ten-year runs of model II. However, different control runs were used for the volcano and $2\times$ CO_2 runs on the one hand and the 18 K run on the other hand so that they paralleled the manner in which sea surface temperature, sea ice, and ocean transport were derived in the various experiments.

We next describe the properties of the volcanic particles that were used in the volcano simulation. Their visible optical depth, τ, was set equal to 0.15 and it was held constant in space over the entire globe and constant in time. This value was chosen to produce a forcing comparable to that of $2\times$ CO_2. The volcanic particles were assumed to be made of concentrated sulfuric acid (75% H_2SO_4 by weight). Thus, they are very good scatterers of solar radiation and very good absorbers of thermal radiation (Pollack and Ackerman 1983). We employed a bimodal, lognormal function to describe their size distribution, with the volume modal radii equal to 0.2 and 0.6μ, and with the widths, σ, equal to 1.6 and 1.2, respectively. These choices of composition and size distribution are based on the measured properties of the El Chichón volcanic cloud (e.g., Hofmann and Rosen 1983; Oberbeck et al. 1983). They are also consistent with properties being derived for the recent Pinatubo volcanic cloud (e.g., Deshler et al. 1992; Valero and Pilewskie 1992) and ones characterizing less well-observed, earlier volcanic clouds (Toon and Pollack 1982).

Each mode was assumed to contribute equally to τ and the volcanic particles were evenly divided between the upper two dynamical levels of the GCM. These properties of the volcano cloud are in approximate accord with properties of the El Chichón volcanic particles during much of its lifetime in the lower stratosphere (Oberbeck et al. 1983; McCormick et al. 1984).

We used Mie theory in conjunction with the optical constants of sulfuric acid (Palmer and Williams 1975) and the above size distribution to evaluate the single scattering properties of the volcanic particles. Since these particles are in a liquid phase (e.g., Oberbeck et al. 1983), the use of Mie theory is appropriate. These choices led to the model volcanic cloud inducing a net cooling of the troposphere and surface, in accordance with the theoretical and observational studies cited in the Introduction.

The radiative calculations in the GISS GCM utilized the correlated k distribution to compute gaseous absorption and a single Gauss point adaptation of the doubling and adding method to compute multiple scattering by clouds and aerosols (Hansen et al. 1983). The thermal infrared calculations used 25 spectrally noncontiguous k intervals to cover the infrared spectrum (see Lacis and Oinas 1991, for a comparison of the correlated k distribution results to line-by-line thermal cooling rates). Each k interval is characterized by a mean absorption coefficient for each gas species that has contributed to this interval and a fraction of the spectrally integrated Planck blackbody function. These two pieces of information were obtained by mapping wavelengths having similar gas absorption coefficients into a given interval and weighting their

contributions by the Planck function. This mapping was performed for H_2O, CO_2, CH_4, and N_2O and used to construct a large table, which was interpolated in pressure, temperature, and gas amount to determine gas optical depths.

Similar tables with 25 spectrally noncontiguous k intervals were generated from the spectral dependence of the Mie scattering cross sections of cloud particles, tropospheric aerosols, and volcanic aerosols. Two cloud types were included: those with 10-μm radius liquid water particles and those with 25-μm effective radius ice spheres to simulate cirrus cloud radiative properties (Hansen and Pollack 1970). Tropospheric aerosols (kept fixed in the experiments conducted here) were also included and were based on the compositions and vertical distributions given by Toon and Pollack (1976). For clouds, a parameterized correction was included to correct the outgoing radiation from clouds for multiple scattering effects.

The radiative treatment for solar radiation used the correlated k distribution (weighted by the solar spectrum) in 15 noncontinuous spectral intervals to compute absorption by H_2O, CO_2, and O_2 and utilized the parameterized O_3 absorption of Lacis and Hansen (1974). Six contiguous spectral intervals were used to model the spectral dependence of cloud and aerosol scattering properties. These included spectrally weighted extinction cross sections, single scattering albedos, and asymmetry parameters for the individual cloud and aerosol species, obtained from Mie calculations. A single Gauss point adaptation of the doubling and adding method, with the "extra angle" formulation to provide explicit zenith angle dependence (Hansen and Lacis 1974), was used for the cloud and aerosol multiple scattering calculations. The solar zenith angle dependence of both clouds and volcanic aerosol was further parameterized by adjusting the upward-to-downward scattering ratio to yield the same zenith angle dependence for the reflected radiation for characteristic optical thicknesses as obtained with the full angle integration of the unparameterized doubling and adding calculations.

Thus, the radiative method provided a self-consistent treatment of the solar and thermal components of the radiative energy balance and included physically realistic multiple scattering interactions among the surface, clouds, and aerosols. While most of the radiative forcing by volcanic aerosols was produced by reflected solar radiation, absorption of upwelling surface thermal radiation produced some counterbalancing greenhouse warming and also generated local stratospheric warming. To a lesser degree, the lower stratosphere was also warmed by absorption of sunlight within the near-infrared bands of sulfuric acid. This solar warming would have been higher during the earliest phases of the introduction of volcanic material into the stratosphere when visible absorbing dust was present, something that we did not include in our calculations.

3. Results

a. Climatology

Here, we describe the transient and steady-state response of the modeled climate to steady-state forcing by a volcanic cloud and compare these results to the response of the system to forcing by 2× CO_2 and the 18 K boundary conditions. The volcano and 2× CO_2 runs began with the present climate, as simulated with model II. Figures 1a and 1b show the temporal evolution of the globally and annually averaged surface air temperature, $\bar{T}_s$, as a function of time from the application of the volcanic and CO_2 perturbations, respectively. The volcano run takes almost twice as long to reach a steady state as does the 2× CO_2 run. This

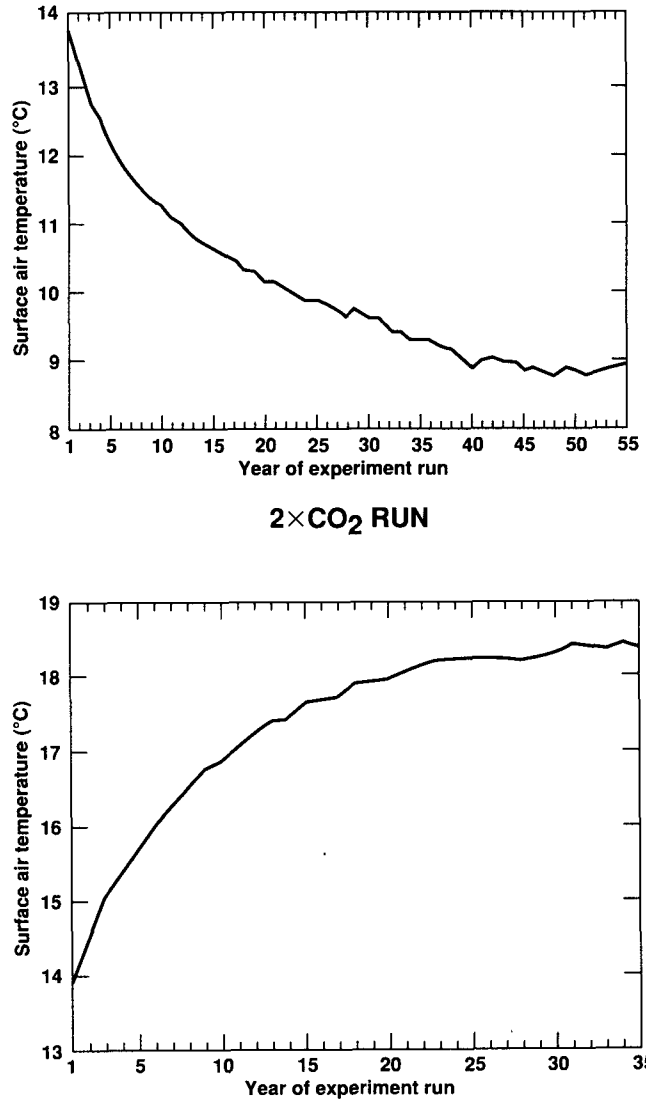

FIG. 1. Globally averaged surface air temperature as a function of time from the start of the simulation for the (a) volcano and (b) 2× CO_2 runs.

difference may in part reflect the T^{-3} dependence of the radiative time constant. In addition, sea ice, by virtue of its very low thermal inertia, played a major role in producing this difference in time scales: sea ice expanded much more in the volcano run than it contracted in the 2× CO_2 run. Thus, finite-amplitude coolings take longer to reach their steady-state asymptotes than do warmings of comparable amplitudes.

The climatology of the volcano run reached an asymptotic steady state during the last part of the simulation, as indicated by the globally averaged net heating at the surface shown in Fig. 2. In particular, this net heating fluctuates about a value of zero during the last ~10 years of the run. A similar behavior was found for the 2× CO_2 run. Thus, we averaged the last ten years of these runs to define the mean steady-state climates produced by their forcings and subtracted these results from similarly time-averaged values for the control run to define the differences between the perturbed climate states and the present state (negative differences in temperature imply a cooler perturbed state).

Figure 3a shows the time and longitudinally averaged surface air temperature difference, ΔT_s, as a function of latitude between the volcano, 2× CO_2, and 18 K runs and their corresponding control runs. These temperature difference curves are far from being identical in absolute value. In particular, the 2× CO_2 profile of ΔT_s is fairly symmetrical about the equator, with the notable exception of its behavior over the Antarctic continent. Also, ΔT_s for 2× CO_2 is smallest at low latitudes and largest at latitudes close to the poles. In contrast, ΔT_s for the volcano run has its smallest absolute value at northern midlatitudes and its biggest absolute value at southern midlatitudes. Also, the values of ΔT_s at high northern latitudes are comparable to those at low southern latitudes. Finally, ΔT_s for the 18 K simulation differs from the volcano run by displaying a strong monotonic increase in absolute value from low to high northern latitudes (due to the presence of continental ice sheets at high latitudes), small values at low latitudes of both hemispheres, and its largest absolute value at high northern latitudes. In both cases, ΔT_s has a sharp feature near 50° to 60°S latitude due to a large increase in sea ice at these locations (see below).

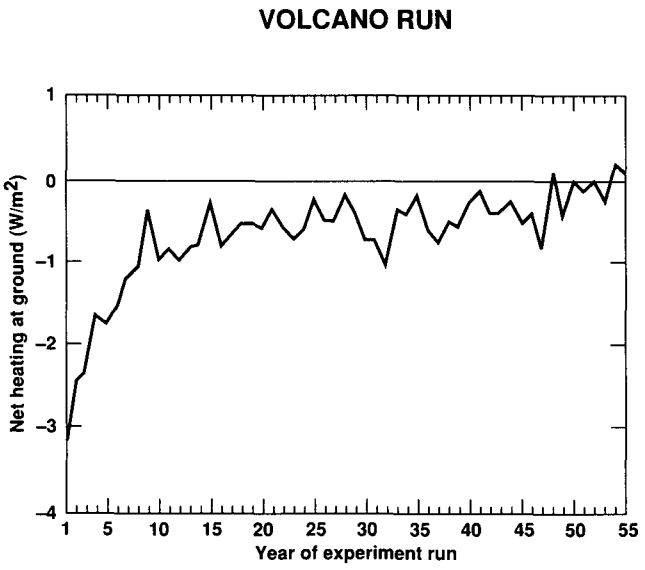

FIG. 2. Globally averaged net heating at the surface as a function of time from the start of the simulation for the volcano run.

Figure 3b shows ΔT_s for the volcano run in units of standard deviation as a function of latitude. The values of the standard deviation were derived from a 100-year control run by computing the rms difference among the values of T_s obtained from ten-year averages of this run. Clearly, all the values of ΔT_s for the volcano run have a high signal-to-noise ratio. The same is true for the values of ΔT_s for the 2× CO_2 and 18 K runs as well as for all the other climatological variables of all three climate simulations.

Figure 3c shows contours of ΔT_s for the volcano run on a latitude/season diagram. Much larger changes occur at high latitudes during the winter than during the summer. A similar seasonal behavior was found for the 2× CO_2 and 18 K runs (paper 2).

Figure 3d exhibits contours of changes in air temperature, ΔT_a, for the volcano run on a pressure/latitude plot. At low latitudes, the largest changes occur within the upper troposphere due to a suppression of penetrative convection and attendant latent heat release aloft. At middle and high latitudes, the largest temperature changes occur close to the surface, since there is less advective heat transport to the higher altitudes at these locations; ΔT_a exhibited similar behavior in the 2× CO_2 and 18 K simulations to that of the volcano run, for much the same reasons (paper 2).

However, important exceptions to the similarity in ΔT_a as a function of pressure and latitude among the three runs include major differences in latitudinal distribution close to the surface, as noted earlier, and important differences in the lower stratosphere. The lower stratosphere cooled by a few degrees at all latitudes in the 2× CO_2 run, due to an enhanced atmospheric emissivity produced by elevated amounts of CO_2. This cooling increased with altitude.

In the volcano run, the lower stratosphere warmed at low latitudes and cooled at high latitudes. These effects are expected to be strongest in the layers in which the volcanic particles resided. The variation in the sign of ΔT_a in the stratosphere with latitude reflects, in part, the importance of the magnitude of the temperature contrast between the lower stratosphere and the generally warmer, underlying troposphere and surface (Pollack and McKay 1985): volcanic particles enhance both the absorption of thermal radiation from other layers of the atmosphere and the emission of thermal radiation from the layers where they are located. When

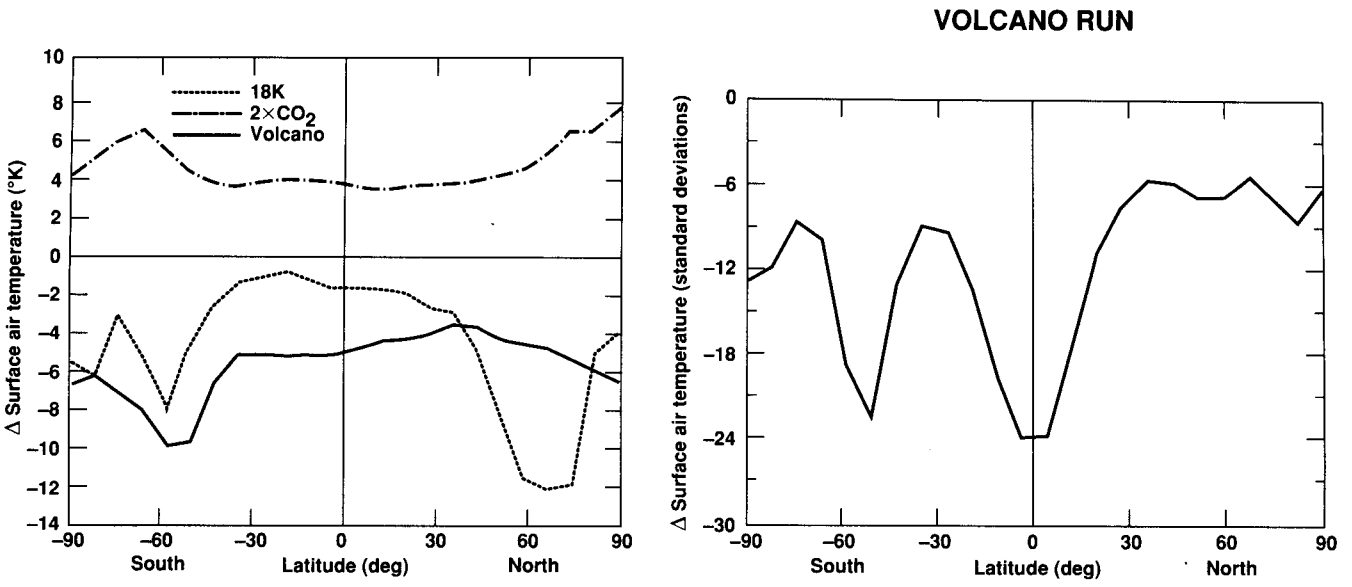

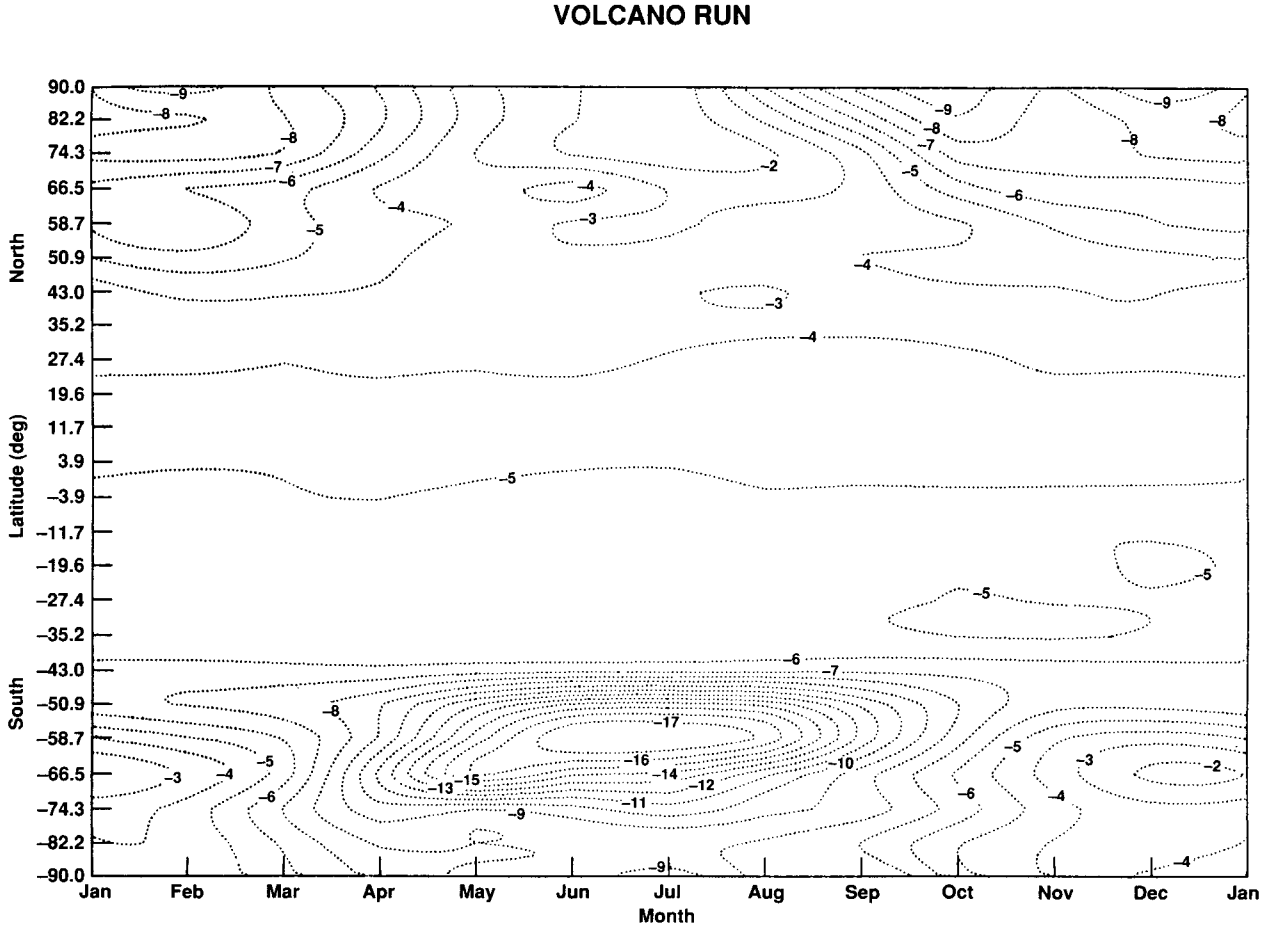

FIG. 3. Annually and zonally averaged change in surface air temperature as a function of latitude for the (a) volcano, 2× CO_2, and 18 K runs in units of K and (b) for the volcano run in units of standard deviation. These figures as well as subsequent ones have been constructed by averaging years 46–55, 26–35, and 2–6 for the volcano, 2× CO_2, and 18 K runs, respectively, and carrying out analogous averages for their control runs. (c) Zonally averaged change in surface air temperature (numbers on contours) for the volcano run as a function of season and latitude. (d) Zonally and annually averaged change in air temperature (contours) for the volcano run as a function of pressure and latitude.

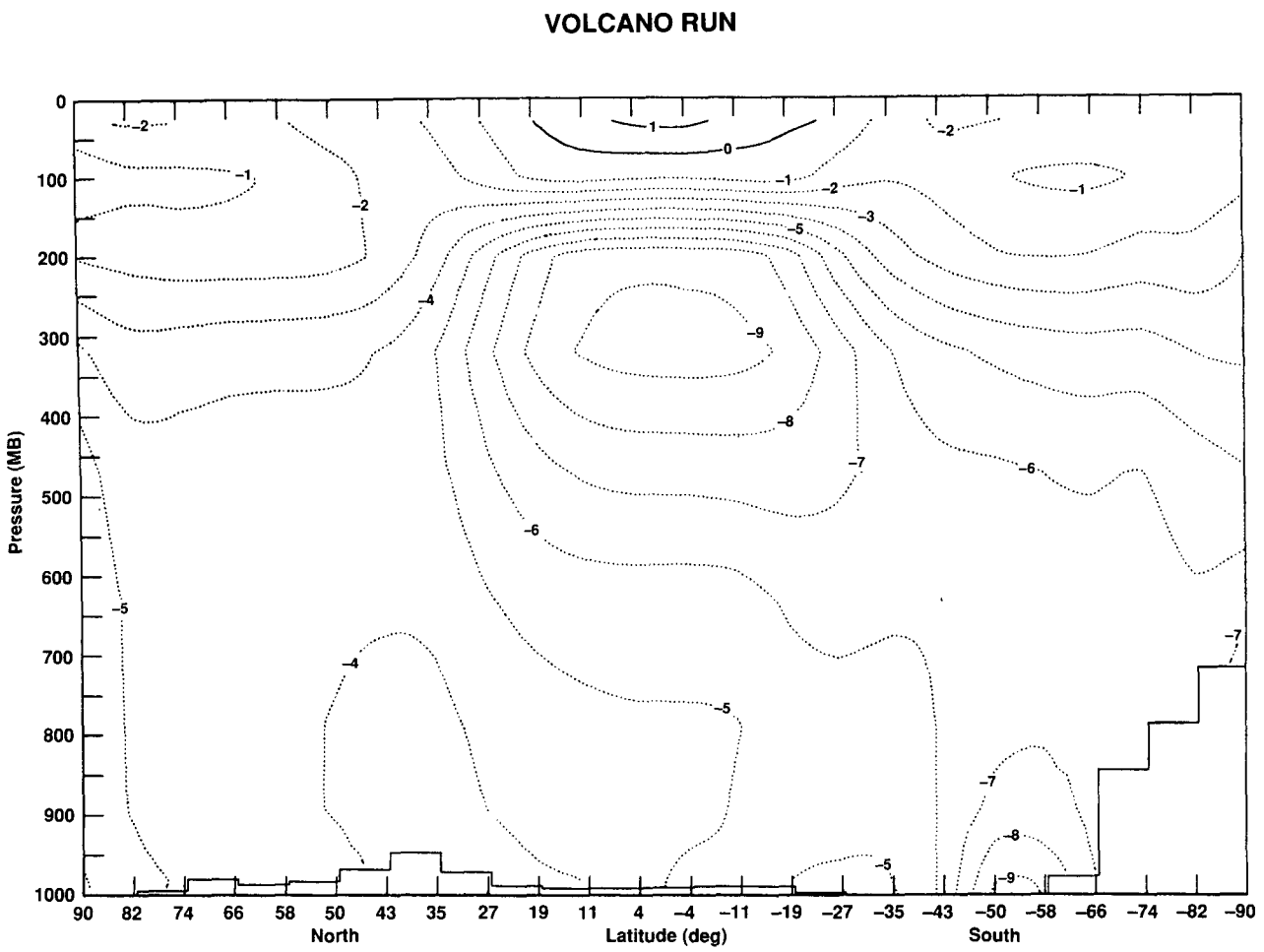

FIG. 3. (*Continued*)

the temperature contrast is large, as it is at low latitudes, thermal radiative exchange causes a net warming. When the temperature contrast is small, as it is at high latitudes, thermal radiative exchange produces a net cooling.

However, both solar radiation and dynamics also affected the temperature changes in the stratosphere in the volcano run. In a companion experiment, the sea surface temperature changes produced in this run and the additional aerosol loading were used in a version of the GISS model that has a better-resolved stratosphere (Rind et al. 1988). This model was then run for three additional years. Analysis of the results indicates that the aerosols altered the solar radiation heating rate to the extent that at the 68-mb level solar heating increased by 0.015 K day^{-1} at low latitudes and decreased by about 0.020 K day^{-1} at high latitudes. The low-latitude effect was caused by absorption within the near-IR bands of sulfuric acid, especially those in the 3- to 4-μm region, while at high latitudes, aerosol scattering at oblique solar incidence angles led to a reduction in radiation. In addition, changes in the residual circulation in the stratosphere cooled the northern latitudes by 0.05 K day^{-1} at 68 mb. Thus, the temperature response of the lower stratosphere to the presence of volcanic aerosols is a result of shortwave, longwave, and dynamical responses. A full discussion of the stratospheric effects and their subsequent effects on the troposphere is contained in Rind et al. (1992).

Finally, temperatures at and slightly above the tropopause in the 18 K simulation did not change at northern mid- and high latitudes, cooled slightly at low latitudes, and warmed somewhat at high southern latitudes. At all these latitudes, ΔT_a tended to 0 with increasing altitude within the stratosphere.

We next consider the changes in surface albedo exhibited by the three runs and their impact on the planetary radiation balance. These changes reflect differences in land snow and sea ice distribution between a given perturbed run and its control run. Figure 4 shows the change in ground albedo, ΔA_s, as a function of latitude. As expected, ΔA_s is almost zero at low latitudes in all three runs and has sizable values at high latitudes. The volcano and 2× CO_2 runs show the largest changes

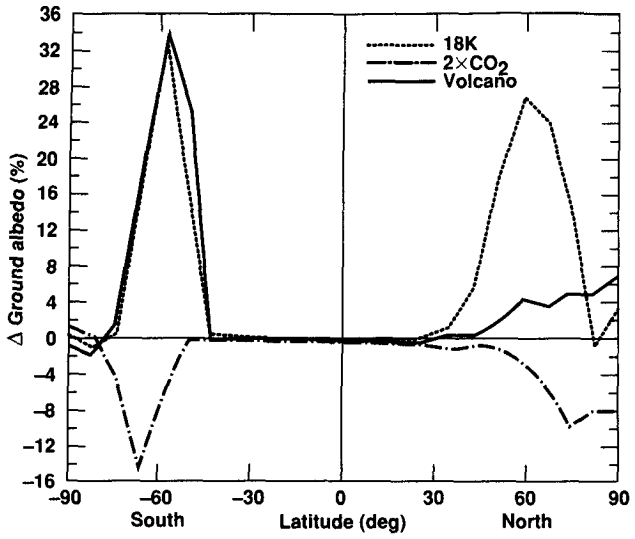

FIG. 4. Annually and zonally averaged change in ground albedo as a function of latitude for the volcano, 2× CO_2, and 18 K runs.

at high southern latitudes, due to the expansion and retreat of sea ice close to the Antarctic continent, respectively. However, both the peak amplitude of ΔA_s and the area of the Southern Hemisphere having sizable values of this parameter are significantly larger for the volcano run than for the 2× CO_2 run, that is, the ice albedo feedback is stronger in a colder climate than in a warmer one. In contrast to these two simulations, the 18 K run not surprisingly exhibits a broad region having large positive values of ΔA_s at mid- and high latitudes of the Northern Hemisphere due to the presence of the large ice sheets on the North American and Eurasian continents. But the 18 K run also shows sizable values of ΔA_s at high southern latitudes, due to a buildup of sea ice, in rough agreement with the profile exhibited by the volcano run at these locations. Since the distribution of sea ice in the 18 K simulations is based on paleoclimatological data, it provides qualitative support for the sea ice distribution obtained for the volcano simulation in the sense that a large response is to be expected at high southern latitudes at times of strong cooling.

Figure 5 shows the change in planetary albedo, ΔA_p, as a function of latitude for the three simulations. These changes illustrate the degree to which the changes in surface albedo of Fig. 4 are reflected in the solar energy budget at the top of the atmosphere. The two sets of curves are not the same, both because some sunlight is scattered back to space by the atmosphere (thus reducing the amplitude of ΔA_p) and because the fraction of cloud cover also changes (thus modulating the shape of ΔA_p). At high latitudes, the shapes of the ΔA_p curves resemble those of the ΔA_s curves, but with amplitudes that are reduced by about a factor of 3 to 4. At low latitudes, the ΔA_p curves are chiefly influenced by the changes in cloud properties, which will be discussed next.

To judge the importance of the values of ΔA_p shown in Fig. 5, one can compare the magnitude of the change in the earth's radiation budget implied by these values with that of the primary forcing. Doubling the atmospheric mixing ratio of CO_2 produces a globally averaged forcing of about 4 W m^{-2}, while changing the globally averaged planetary albedo by 10% is equivalent to a change of 24 W m^{-2} (paper 2). Thus, the surface albedo changes at high latitude and the resulting changes in planetary albedo can be expected to have a significant impact on the final climate state.

Figure 6a shows the time- and longitude-averaged change in cloud cover, ΔF_c, as a function of latitude for the three perturbed runs. In all three cases, the change in cloud cover is spatially well correlated with the change in sea ice at high southern latitudes (e.g., cf. Figs. 4 and 6a). The sense of the correlation is that cloudiness decreases (increases) at latitudes where sea ice increases (decreases). We suggest that the changes in cloud cover at high southern latitudes result in part from a decrease (increase) in evaporation in places of increased (decreased) sea ice. The decrease in evaporation associated with an increase in sea ice is due to the formation of a stable boundary layer over sea ice, which leads to a very large decrease in the vigor of turbulent mixing. The reduced evaporation leads to a reduction in low-level cloud cover.

There are several reasons for our postulating the above set of causal relationships between changes in sea ice and cloudiness at high southern latitudes, aside from their spatial coincidence. First, the low-altitude relative humidity at 60°S (near the center of the sea ice changes) is significantly lower in the volcano run

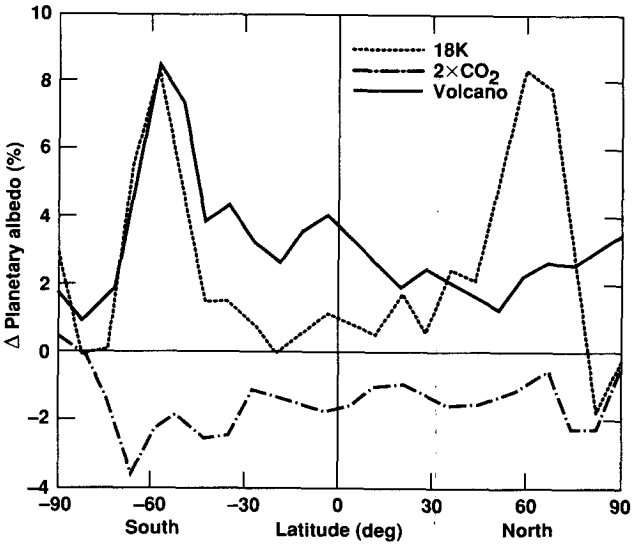

FIG. 5. Annually and zonally averaged change in planetary albedo as a function of latitude for the volcano, 2× CO_2, and 18 K runs.

than it is in the control run. Second, the latitude region of the Southern Hemisphere that encompasses the location of increased sea ice in the volcano run exhibits a reduction of cloudiness at low altitudes, whereas cloudiness at low altitudes increases at almost all other latitudes (cf. Fig. 6b). Furthermore, this reduced, low-altitude cloudiness at high southern latitudes peaks close to the surface.

Changes in atmospheric water vapor transport may have also contributed to the changes of cloudiness at high southern latitudes. In particular, the volcano run exhibits an increase of latent heat divergence due to atmospheric transport at these latitudes (cf. Fig. 12 and the discussion later in the paper) so that changes in water transport favor a decrease in cloudiness.

Alternative explanations for the change in cloud cover at high southern latitudes are not supported by our analysis of the three experiments. In particular, since the extreme latitudinal temperature gradient and, hence, the jet-stream track shift to lower latitudes for the cooling experiments, it might be argued that there is less storminess at the high southern latitudes where there is a buildup of sea ice. But, the eddy kinetic energy does not decrease at these latitudes during southern summer (cf. Fig. 11 and the discussion of these figures later in the paper). Furthermore, the annually averaged eddy kinetic energy increases between 50° and 70°S in the volcano run, with the increase being largest near the equatorward edge of the region of enhanced sea ice. Such increases should imply a more vigorous baroclinicity and may be responsible for the increased cloudiness aloft at high southern latitudes (cf. Fig. 6b).

The ΔF_c curves for the volcano and 18 K are similar but not identical to one another. While the curve for $2\times$ CO_2 is (crudely) a mirror image of the volcano and/or 18 K curves at some of the higher latitudes, especially those in the Southern Hemisphere, it is not even close to a mirror image at the lower latitudes of both hemispheres. Thus, there are marked departures from symmetry in the behavior of the changes in fractional cloudiness between climate warmings and climate coolings and even, to a lesser extent, between different types of climate coolings.

Further insight into some of the factors controlling the ΔF_c curve for the volcano run is provided by Fig. 6b, which shows the change in cloud amount (contours) on a pressure/latitude diagram. In this run, there is a decrease in high-level clouds (cirrus) at all latitudes, with the largest reduction occurring at low latitudes. This reduction is due to changes in the depth and vigor of the large-scale circulation, as well as a reduction in penetrative convection. Cloudiness increased at lower altitudes in the tropics due to an enhanced low-level convection. But, low-level convection cannot increase substantially because colder sea level temperatures limit the associated vertical motions. Thus, the net effect is a reduction in total cloud cover (cf. Fig. 6a).

The 18 K simulation shows similar behavior to the volcano run at low latitudes (paper 2). However, the reduction in high-altitude clouds at low latitudes for the 18 K run was not as great as for the volcano run and the 18 K run exhibited a small increase in high-altitude clouds at high northern latitudes. Presumably this latter change reflects the influence of orographic forcing by the highly elevated ice sheets.

Changes in the large-scale circulation and increased penetrative convection for the $2\times$ CO_2 simulation result in an increase in high-altitude clouds. Quite conceivably, the GISS model may underestimate the increase in high-altitude cloudiness in this experiment, since clouds are not allowed to form above 100 mb. Indeed, $2\times$ CO_2 experiments conducted with GCM models that permit clouds to form above 100 mb show a small percentage increase in cloud amount above 100 mb in the tropics (Wetherald and Manabe 1988). A decrease in the vigor of low-level convection results in a decrease in low-altitude clouds at most latitudes. To first approximation, these changes are mirror images of the changes in cloudiness found for the volcano run. However, there are some differences. For example, high-altitude cloudiness decreased at low southern latitudes in the $2\times$ CO_2 run (but see the caveat above on clouds not being able to form above 100 mb). Also, the altitude-integrated changes in cloud cover are not mirror images of one another in the tropics, as noted above (cf. Fig. 6a). We do not think that this latter asymmetry is a result of limitations in the GISS model as to where clouds can form, since $2\times$ CO_2 experiments with GCMs that allow clouds to form above 100 mb also show a decrease in total cloud cover in the tropics (Wetherald and Manabe 1988). The role of atmospheric dynamics in producing some of these changes will be discussed in a later section of this paper.

Finally, Fig. 6c shows the change of total cloud cover for the volcano run as a function of season and latitude. The strongest seasonal variations are found at the highest latitudes, as might have been expected. But perhaps a bit surprisingly, the seasonal variation is fairly muted at middle latitudes, especially in the Southern Hemisphere.

b. Feedbacks

We have used a two-dimensional radiative–convective model to analyze the feedback effects in the GCM simulations. There are two primary reasons why we used this approach, rather than conducting this analysis directly with the 3D model. First, we are not as limited by the noise inherent in the GCM (as also occurs in the real world) in defining the relationships between individual climate factors and the response of the climate system. Second, it would have involved a prohibitively large amount of computer time to determine each of the feedback factors, especially for long runs such as the volcano and $2\times$ CO_2 simulations. A 1D radiative–convective model was used in paper 2 to de-

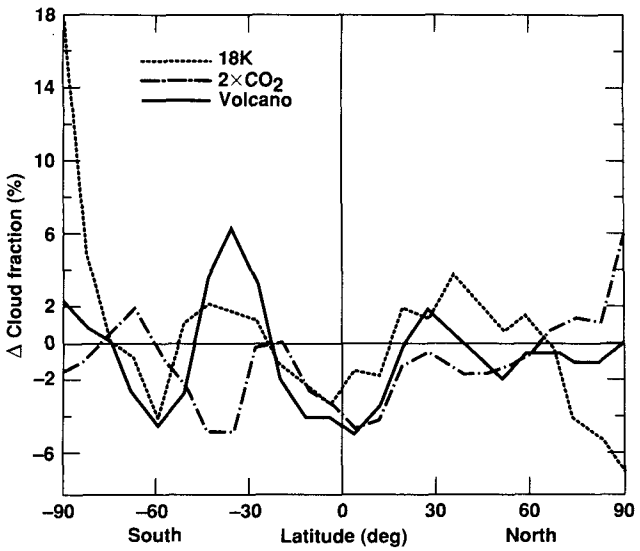

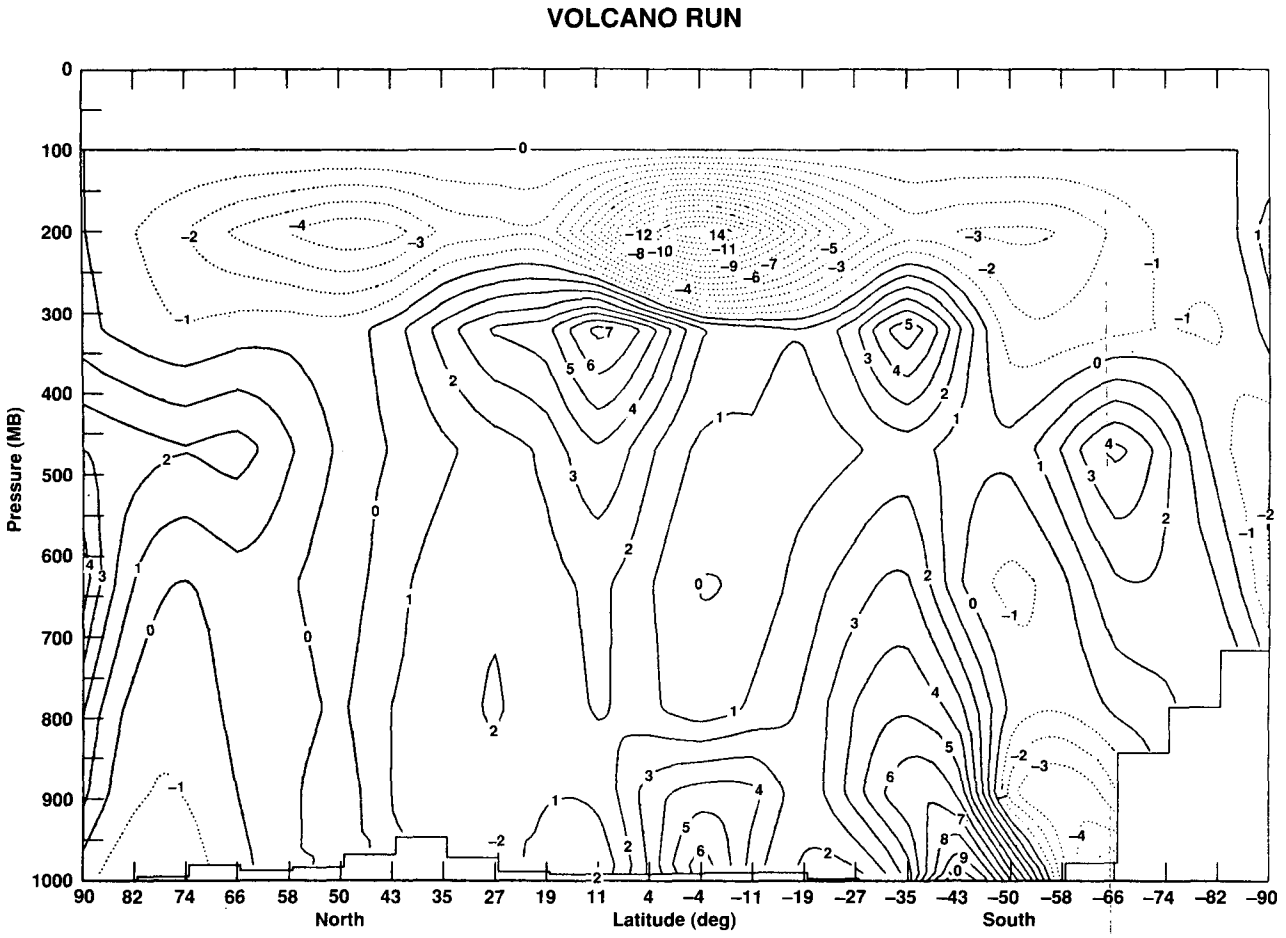

FIG. 6. (a) Annually and zonally averaged change in percentage cloud cover as a function of latitude for the volcano, 2× CO_2, and 18 K runs. Contours of the change in percentage cloud cover for the volcano run in a pressure/latitude diagram (b) and a latitude/season diagram (c).

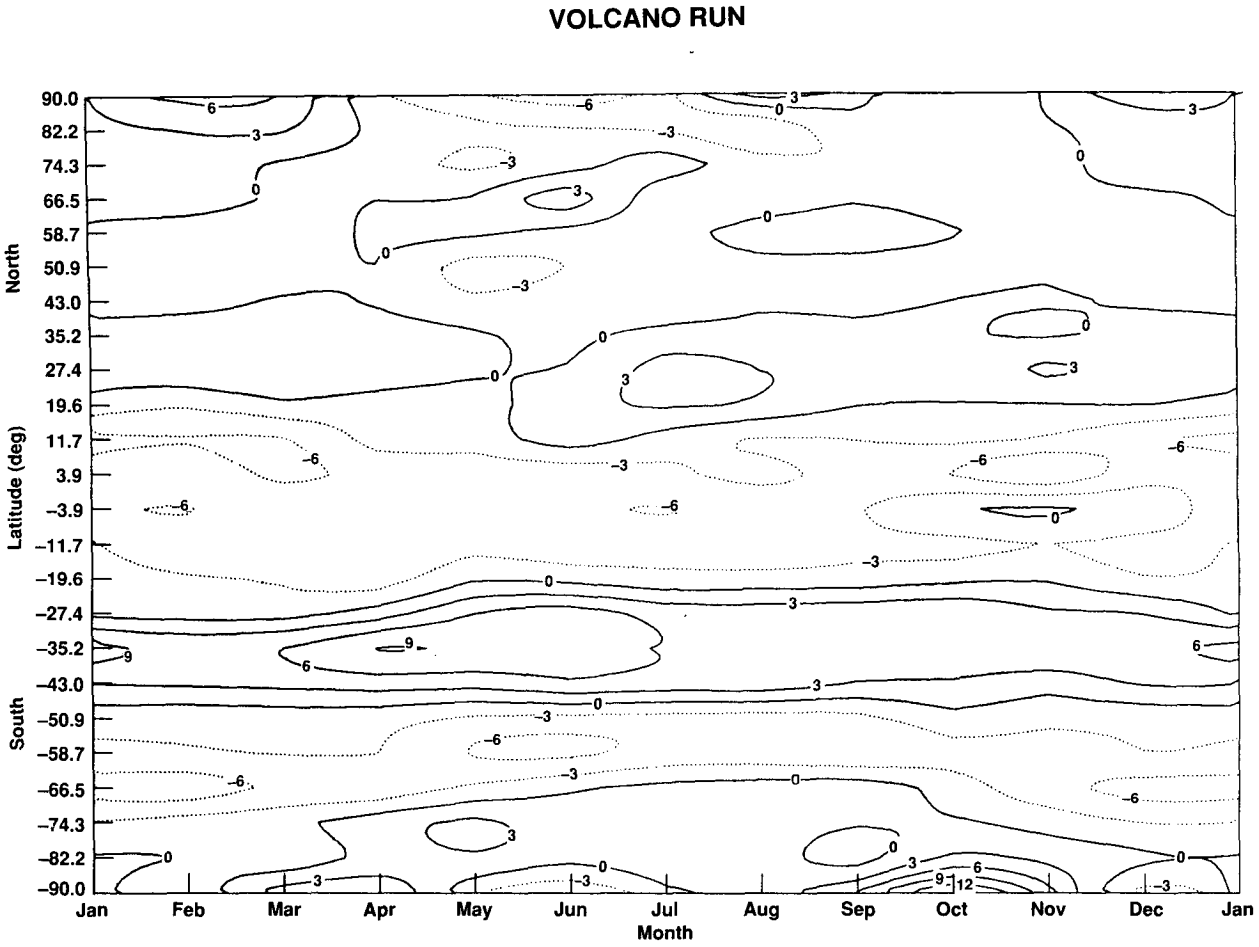

FIG. 6. (*continued*)

termine globally averaged feedback factors. Here, we employ a 2D model of this type to determine the latitudinal dependence of the feedback factors and to examine the influence of dynamical as well as radiative factors.

The 2D radiative–convective feedback model computes the equilibrium atmospheric temperature profile and the ground temperature at each latitude by performing a detailed energy balance calculation. It does so using annually and zonally averaged parameters from the GCM simulations and algorithms analogous to ones used in the GCM. In particular, the 2D model employs the same radiative transfer code that is used in the GCM. The 2D model considers solar and thermal radiative heating, the convergence of atmospheric meridional transport of sensible, latent, and geopotential energy, and the convergence of oceanic meridional heat transport. The 2D model is time marched to a steady-state temperature profile at each latitude.

The 2D model obtains the dynamical heating terms directly from the GCM results. It also obtains atmospheric and surface parameters from the GCM that are needed for calculating radiative heating rates. These include the vertical profiles of water vapor, other radiatively active gases, clouds, and atmospheric aerosols, the temperature lapse rate, and the surface albedo. The GCM provides information on the fraction of cloudiness in each atmospheric layer and, in particular, cloud fractions of low-, middle-, and high-level clouds, as well as the clear-sky fraction for the entire vertical column. Since the sum of the GCM low, middle, high, and clear fractions is greater than unity, overlapping cloudiness occurs and needs to be allowed for. We do so in the 2D analysis by defining an overlapping cloud category consisting of equal amounts of low, middle, and high clouds such that the sum of nonoverlapped and overlapped cloud fractions is equal to 1 minus the clear-sky fraction. In addition, we uniformly adjust the column cloud optical thickness to match the annually averaged planetary albedo of the GCM results. Thus, details of the diagnostic information that are not directly available from the GCM output are extrapolated from available information using a minimum of assumptions to define the radiative input for the 2D model analysis of GCM control and experiment data.

First, a reference temperature structure is calculated

by using parameter values from the control run and time marching the 2D model to an equilibrium state. This structure is always quite close to that obtained directly from the GCM output. We calculate the annually and zonally averaged temperatures, rather than directly use the GCM results, so as to treat the control run in the same way that we treat climate perturbations. Next, information is used selectively from an altered climate run (e.g., the 2× CO_2 experiment). The value of only one climate factor (e.g., atmospheric water vapor) is obtained from the altered climate run and the values of all the remaining variables are taken from the control run. The 2D model is again run to equilibrium. The difference in temperature of the air at the surface, ΔT_s, between the 2D perturbed and 2D reference cases provides a measure of the influence of a given climate variable in producing the total temperature change found in the altered climate run with the GCM. Values of ΔT_s are obtained for all the climate variables. One can also readily obtain the system's gain, g, which is simply the fraction of the total temperature change produced by a given climate variable (paper 2). (We deviate a bit from the convention used in paper 2 in that we also evaluate g for the primary forcing variable as well as all the feedback factors.)

In using the 2D model to isolate the contribution of each key climate variable to the altered climate state, we are making three assumptions. First, we assume that the use of zonally and annually averaged information is adequate for computing zonally and annually averaged temperature changes. Second, we assume that the lack of complete cloud information in the GCM output (see above) will not seriously alias our final results. Third, we assume that the total temperature change can be well represented by the sum of the changes produced by each climate variable in isolation.

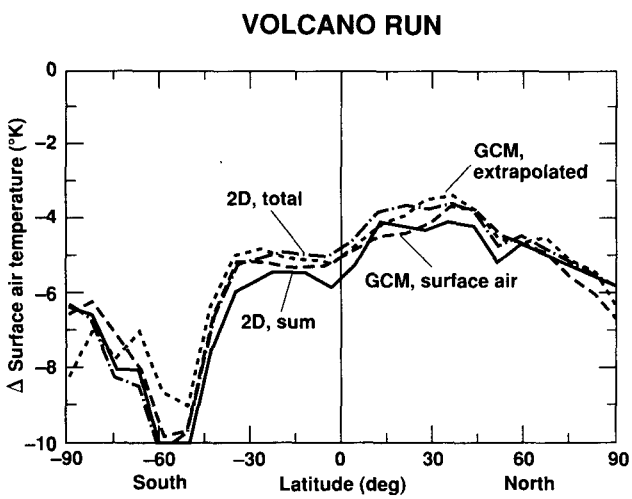

FIG. 7. Comparison of the summed and total changes in annually and zonally averaged surface temperature given by the 2D radiative/dynamical model with analogous temperatures given by the GISS Climate Model II (GCM) for the volcano run. The term "summed" refers to adding up the changes in temperature when each variable is changed individually, while the term "total" refers to the change in temperature when all the variables are altered simultaneously. The two GCM curves refer to results obtained directly from calculated surface air temperatures and by extrapolating from the midpoints of the lowest two model layers.

Some confirmation of the approximate validity of the above assumptions is shown in Fig. 7, where we compare the total temperature changes given by the 2D model with those obtained directly from the GCM volcano run. Two curves are shown for the total temperature change found by alternately using the surface air temperature and the value found by extrapolating the values at the midpoints of the two lowest layers of the atmosphere to the ground. Since the 2D model does not have a boundary layer, it is not clear which of these two GCM values is the most appropriate one to compare with the 2D value. Two additional curves are shown to indicate the total temperature changes found with the 2D model by alternately summing the temperature changes produced by climate variables that are varied one at a time from their control values and temperature changes obtained when all the climate variables are permitted to change simultaneously. We see that all four curves lie close together. Similar results were obtained for the 2× CO_2 and 18 K runs. Thus, the 2D results can be expected to provide useful representations of the complete GCM simulations and the net change produced by the cumulative changes in all the variables is closely approximated by the sum of the changes produced by each variable separately.

Figures 8a and 8b show ΔT_s as a function of latitude for the primary radiative forcing variable and for the four major secondary climate variables that collectively determine the climate changes that occurred in the volcano and 2× CO_2 runs. Figure 8c displays analogous information for the four major secondary variables of the 18 K run. As mentioned earlier, both the 18 K run and its associated control run had fixed sea surface temperature and sea ice. Thus, this case lacks a well-defined primary forcing variable, other than the boundary conditions themselves. Figures 8d, 8e, and 8f show the system's gain, g, for the primary and secondary variables of the three climate experiments, where g is simply ΔT_s for a given variable divided by the total ΔT_s (Hansen et al. 1984). Although the same information is used to construct Figs. 8a–c and 8d–f, they serve complementary functions: Figs. 8a–c define the magnitude and sign of ΔT_s due to a given variable (as well as the total), while Figs. 8d–f define the fractional contribution of a given variable to the total change. This latter presentation makes it easier to compare the impact of a given variable in each of the three experiments. Note that the shapes of comparable curves are somewhat different in the two forms of presentation since the total ΔT_s, as well as the individual ΔT_s, varies with latitude (also, the sign will differ when the total ΔT_s is negative).

The curves labeled "aerosol" and "CO_2 only" in Fig. 8 show the direct effects of the radiative forcing by volcanic particles and enhanced CO_2 for the volcano

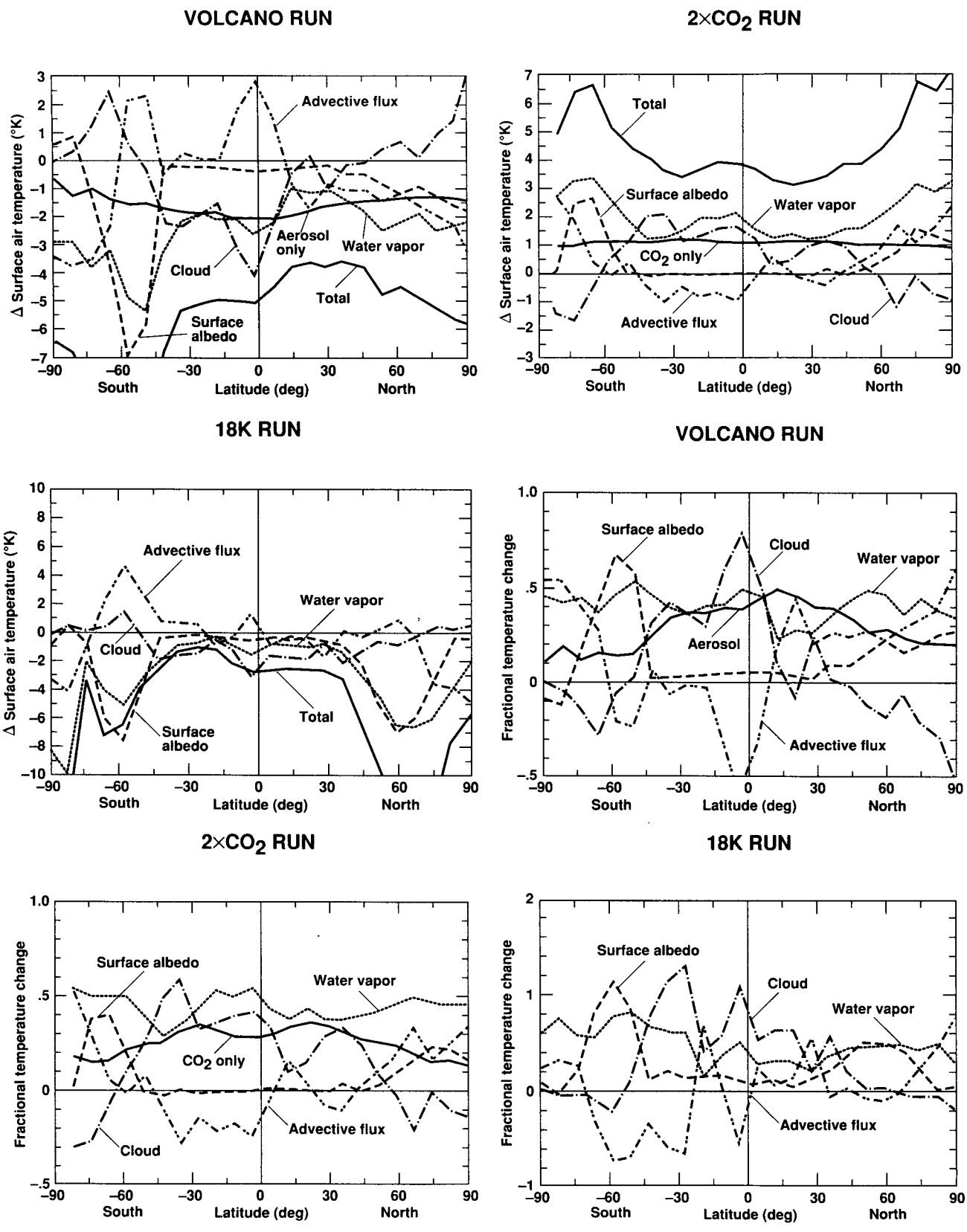

FIG. 8. Annually and zonally averaged change in surface temperature due to the primary radiative drive and various feedback factors for the volcano [(a) and (d)], 2× CO_2 [(b) and (e)], and 18 K [(c) and (f)] runs. In (a)–(c), these changes are expressed in units of K, while in (d)–(f) they are expressed as fractions of the total change.

and 2× CO_2 runs, respectively. The major categories of secondary climate variables that vary between the control and perturbation runs and that alter the response of the climate system include atmospheric water vapor, clouds, surface albedo, and heat advection. The first three of these secondary variables directly affect the radiation balance in different ways. Since oceanic heat advection is kept constant between the volcano and 2× CO_2 runs and their control runs, it does not directly alter the magnitude of the climate changes occurring in these two cases. Thus, the advective flux refers only to atmospheric heat transport in these cases. However, oceanic heat advection did vary between the 18 K run and its control run, so that the advective flux in Figs. 8c and 8f refers to the impact of the change in heat advection by the atmosphere plus the ocean.

The direct volcanic aerosol forcing produces a cooling of about 2 K at the equator and only about 1 K at the highest latitudes (cf. Fig. 8a). By contrast, the direct CO_2 forcing produces an almost constant warming of 1 K (cf. Fig. 8b). The difference in the latitudinal dependence of these two radiative forcings reflects differences in the components of the radiation field that the two variables are affecting and their altitude profiles. The radiative forcing by CO_2 is restricted almost entirely to the thermal portion of the spectrum. Carbon dioxide is uniformly mixed throughout the atmosphere and has important effects on the thermal radiative heating rates in both the troposphere, where it causes a net warming, and the stratosphere, where it causes a net cooling (paper 2). In contrast, volcanic dust affects both solar and thermal radiation, with the solar impact dominating in the troposphere, except at high latitudes during winter. Thus, its direct forcing is largest at low latitudes, where the annually averaged amount of sunlight is largest. At high latitudes, the direct aerosol forcing produces a net warming during winter when the sun is below or close to the horizon. During other times of the year, the solar cooling effect at high latitudes is diminished by having a high albedo surface underlying the volcanic particles and is enhanced by having a larger slant path than at low latitudes. When averaged over a year, a diminished net cooling occurs at high latitudes.

Direct volcanic forcing accounts for about 30% of the total globally averaged temperature change, while CO_2 forcing accounts for about 25% of the total (cf. Figs. 8d and 8e). Thus, there is a slightly larger amplification of the direct forcing in the 2× CO_2 run. The situation is less clear-cut for the 18 K simulation, in the sense of defining unambiguously the variable(s) that are providing the primary forcing of the ice age climate (paper 2). On the one hand, if only the annually and globally averaged insolation changes associated with the Milankovitch orbital changes are considered, then the direct forcing accounts for only a tiny fraction of the total climate change ($\approx$5%). On the other hand, if climate variables that operate on long time scales—land ice, CO_2, and vegetation—are included among the primary drives for the ice age climate, then collectively they account for about 25% of the globally averaged temperature change, a value quite similar to that for the volcano and 2× CO_2 runs.

Water vapor provides a major, positive amplification of the temperature changes at all latitudes in all three climate experiments, primarily by altering the amount of greenhouse trapping of thermal radiation. According to Figs. 8d, 8e, and 8f, changes in atmospheric water vapor account for about 45% of the total globally averaged temperature change in the volcano and CO_2 runs, but only about 25% of the total change in the 18 K case. Thus, changes in water vapor represent the most important feedback mechanism in the first two cases, while changes in cloud properties have a comparable importance to changes in water vapor for the 18 K case.

As discussed in paper 2, the total impact of water vapor on an altered climate state can be subdivided into the impact due to changes in the vertically integrated amount of water vapor in the atmosphere, changes in its vertical distribution, and changes in the atmospheric lapse rate, which water vapor induces by latent heat release. Figures 9a, 9b, and 9c show such a dissection of the water vapor impact by displaying the total fractional change in temperature due to water vapor variability (chain curve), change in the column abundance of water vapor (column: solid curve), change in both column abundance and vertical distribution (profile: dotted curve), and change in lapse rate (lapse rate: dashed curve). We determined the impact of changes in column, profile, and lapse rate by changing the water vapor abundance at each altitude by the same fractional amount as that experienced by the entire vertical column, by changing the abundance individually for each layer by an appropriate amount, and by changing the lapse rate in accordance with the GCM results.

According to Fig. 9, the total change and the change due to a varying column abundance track one another quite closely at low and middle latitudes, with the changes due to water vapor distribution (the difference of the dotted and solid curves) and lapse rate tending to have comparable amplitudes and opposite signs. However, at high latitudes, the three separate factors induce changes having the same sign, so that the total change significantly exceeds that due solely to the change in column abundance.

Recent analyses of satellite measurements have provided strong support for the basic validity of the water vapor feedback predicted by GCMs. Raval and Ramanathan (1989) analyzed long wavelength fluxes measured by the ERBE satellites over open oceans for cloud-free conditions. They showed that the correlation between the greenhouse effect (the difference between the upward IR fluxes at the surface and top of the atmosphere) and surface temperature was quantitatively very similar to that predicted by several GCMs and to

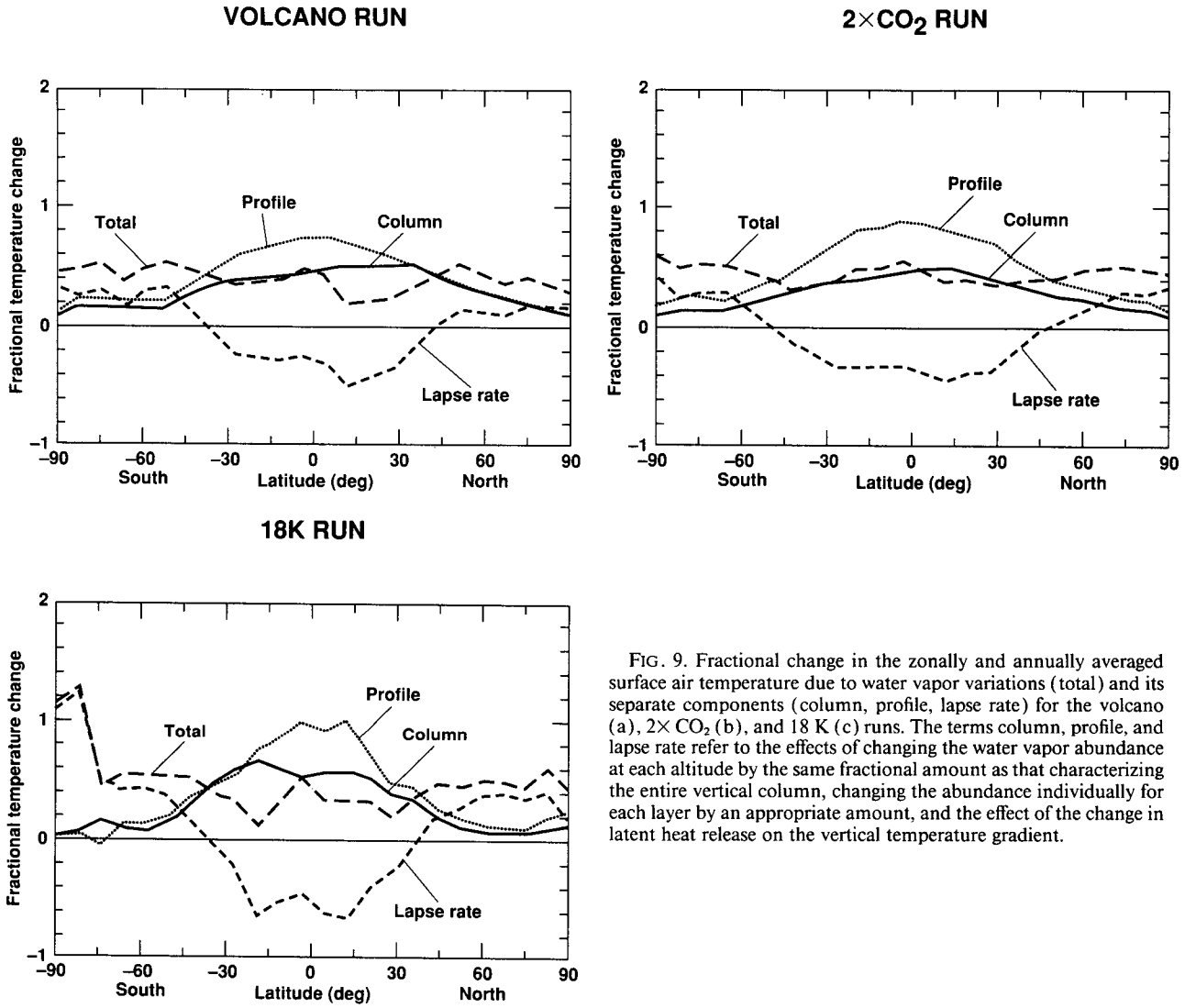

FIG. 9. Fractional change in the zonally and annually averaged surface air temperature due to water vapor variations (total) and its separate components (column, profile, lapse rate) for the volcano (a), 2× CO_2 (b), and 18 K (c) runs. The terms column, profile, and lapse rate refer to the effects of changing the water vapor abundance at each altitude by the same fractional amount as that characterizing the entire vertical column, changing the abundance individually for each layer by an appropriate amount, and the effect of the change in latent heat release on the vertical temperature gradient.

that expected from changes in the column abundance of water vapor, as controlled by its saturation vapor pressure curve. The results shown in Fig. 9 provide additional perspective on this most important finding. At the low and middle latitudes examined by Raval and Ramanathan, that is, places free of ocean ice, the water vapor feedback is plausibly dominated by changes in the column abundance of water vapor. However, there is not an exact cancellation of the feedbacks due to changes in the vertical distribution of water vapor and the lapse rate. Furthermore, the net water feedback deviates substantially from that of the column component alone at high latitudes. These components are both harder to measure and more difficult to predict, although there seems to be a strong consensus among climate GCMs on the nature and strength of the water vapor feedback, despite their considerable disagreements on cloud and other feedbacks (Cess et al. 1989).

Additional support for the validity of GCM-predicted feedbacks due to water vapor was provided by Rind et al. (1991). They used measurements of water vapor obtained from the SAGE II satellite experiment to evaluate seasonal and regional variations of absolute and relative humidity. They found that at warmer times of the year and in warmer locations, the absolute humidity strongly increased at middle and high altitudes of the troposphere, while the relative humidity slightly increased. These results are qualitatively and quantitatively in good accordance with those expected from standard treatments of penetrative convection and the predictions of the GISS climate model, but they are totally inconsistent with the expectations of an alternative model of penetrative convection (Lindzen 1990). This comparison, therefore, provides some support for the validity of the changes in both column abundance and vertical distribution of water vapor predicted by climate GCMs in general and the GISS

model in particular. Thus, they support the predicted feedbacks due to these two components of the water feedback.

Changes in surface albedo provide a strong, positive feedback at high latitudes in all three altered climate cases. In the volcano and $2\times CO_2$ runs, the changes in surface albedo result almost entirely from changes in the amount of sea ice. In the 18 K experiment, changes in the amount of sea ice near 60°S latitude induce sizable albedo and temperature changes, while the large increase in land ice, that is, ice sheets, in the Northern Hemisphere results in temperature changes having a comparable peak amplitude and a broader latitudinal extent than that due to sea ice in the Southern Hemisphere (Fig. 8f). A minor contribution also originates from albedo variations associated with changes in vegetation. These differences in the source of the altered surface albedo among the three experiments are reflections of differences in time scale. Sea ice changes much more rapidly ($\approx$ decades) than does land ice in the form of mobile glaciers ($\approx$ millenia). But, note that there are also longer time scales for changes in sea ice that are associated with changes in the circulation of the deep oceans—these longer time scale changes are not encompassed or explicitly modeled by the variable sea surface temperature (SST) experiments discussed in this paper.

According to Figs. 8d–f, clouds produce a positive feedback at low latitudes and a negative feedback at high latitudes in all three altered climate runs, although the transition from positive to negative feedback occurs at somewhat different latitudes in each of the various experiments. Remarkably, most of the cloud feedback at each latitude in these three experiments is cancelled by feedbacks of opposite sign due to heat advection. This near-cancellation of these two feedback effects is most completely realized for the $2\times CO_2$ run and least completely realized for the 18 K run. Also, it is poorly realized in both the volcano and 18 K runs at high southern latitudes, where there is a significant expansion of sea ice.

Differences in the degree of cancellation of the cloud and advective feedbacks between the volcano and $2\times CO_2$ runs on the one hand and the 18 K run on the other hand could reflect, in part, important differences in the nature of these experiments. There is no ocean transport feedback in the first two of these runs, but there is an implied one for the 18 K experiment. However, there are reasons for suspecting that the CLIMAP sea surface temperatures that were used in the 18 K run may be somewhat too large in the tropics—1 to 2 K (paper 2; Rind and Peteet 1985; Broccoli and Manabe 1987)—and, hence, the ocean feedback is correspondingly uncertain.

In the GISS GCM, cloud feedback can arise from changes in cloud cover, cloud altitude, column thickness, and diurnal variability, but not from cloud microphysical or optical thickness changes. An increased optical thickness of low clouds would produce a negative feedback component that is missing in the GISS GCM, but since most cirrus clouds are optically thin, an increase in cirrus cloud optical thickness could produce a positive cloud feedback; their enhanced greenhouse warming of the surface might exceed their enhanced solar reflectivity.

Obviously, the cloud prediction scheme in the GISS GCM is very crude, as is the case for all current GCMs. The GCM intercomparison by Cess et al. (1990) shows cloud feedbacks varying from strongly negative to neutral to strongly positive.

Ramanathan and Collins (1991) carried out pioneering analyses of ERBE observations in an attempt to define the sign and magnitude of the cloud feedback. In particular, they compared the solar and thermal (or greenhouse) cloud forcings over the tropical Pacific Ocean for an El Niño year (1987) with those for non–El Niño years (1985 and 1989). They found a striking spatial correlation among locations having elevated SSTs, enhanced solar reflected fluxes, and enhanced greenhouses. The changes in solar and thermal cloud forcings between the El Niño and non–El Niño years were found to be linearly correlated, with the slope of the correlation implying a modest dominance of the solar effect, that is, the clouds produced a net negative feedback. Ramanathan and Collins therefore suggested that there was a direct causal relationship between elevated SSTs in the tropical Pacific and enhanced, negative cloud feedbacks involving cirrus anvils.

If the above study is accepted at face value, it defines at best the cloud feedback relationships at very low latitudes. Even in this restricted sense there is some ambiguity about the sign of the net radiative effect of clouds: the correlation between the absolute solar and thermal cloud forcings for the individual years implies a slightly positive net cloud feedback (Ramanthan and Collins 1991).

A very recent study by Fu et al. (1992) casts some doubts on the results and implications of the study by Ramanathan and Collins (1991). Fu et al. (1992) deduced the impact of cirrus clouds on solar and thermal radiation from International Satellite Cloud Climatology Project (ISCCP) radiance data. They argued that the changes in cloud forcing found by Ramanathan and Collins (1991) were not due to changes in SSTs. For example, changes in solar and thermal cloud forcings between two non–El Niño years with minimal differences in SSTs were found to be very similar to those between an El Niño year and a non–El Niño year. Also, there were no significant systematic changes in solar or thermal cloud forcings between 1987 and 1985 when these changes were averaged over the entire tropical Pacific basin, even though the basin-averaged SSTs were larger during the El Niño year. The analyses of Fu et al. (1992) also indicated that the variations in cloud forcing, when averaged over large spatial scales, were due chiefly to changes in fractional cloudiness

rather than cloud reflectivity or cloud-top temperature and that changes in the large-scale Walker and Hadley circulations were the chief sources of the variable cloud forcings.

Thus, cloud feedbacks remain poorly modeled and poorly understood. Nevertheless, satellite data are becoming available to address this important issue, as exemplified by the studies of Ramanathan and Collins (1991) and Fu et al. (1992). Further analyses of other natural, short-term climate changes and seasonal variations over a wide range of latitudes can help to improve matters substantially on the observational side, while the development and verification of schemes for parameterizing changes in cloud optical properties in GCMs may make their predictions of cloud feedbacks more believable in the future.

c. *Dynamics*

The conventional view of climate change is that high latitudes will be more sensitive than low latitudes. Therefore, as the climate cools, high latitudes will cool more than low latitudes, increasing the latitudinal temperature gradient. With increased latitudinal temperature gradients, baroclinic instability and eddy energy should increase, enhancing eddy and atmospheric energy transports. Thus, the response of the dynamics to climate change in this scenario is to provide a negative feedback by warming the latitudes that are cooling the most.

The results from the volcano run are in direct contradiction to *all* of the above statements. First, high latitudes do not cool significantly more than low latitudes, especially in the Northern Hemisphere, as has already been pointed out for annually averaged conditions (cf. Fig. 3a). This matter is further explored in Fig. 10a, which shows the latitudinal distribution of ΔT_s for the winter season in the Northern Hemisphere, the time of most vigorous atmospheric dynamics for that hemisphere. Besides displaying ΔT_s for the volcano run, this figure also shows the corresponding curves for the 2× CO_2 and 18 K runs. In contrast to the results for the other two runs, ΔT_s for the volcano run *decreases* from low to midlatitudes in the Northern Hemisphere. While ΔT_s for the volcano run then increases from northern mid- to high latitudes, its values at high latitudes are generally less than those for the other two runs. As discussed in more detail at the end of this subsection, the large differences in the ΔT_s latitudinal profiles of the three runs are caused, in gross detail, by variations in the latitudinal profiles of the primary radiative forcing (cf. Figs. 8a–c) and, in fine detail, by the radiative and dynamical responses to this forcing. Here, we focus on the dynamical responses to the ΔT_s profiles to set the stage for this later discussion.

Several processes produce a high-latitude amplification of ΔT_s when the climate warms, as illustrated by the results for 2× CO_2 in Fig. 10a. The high stability

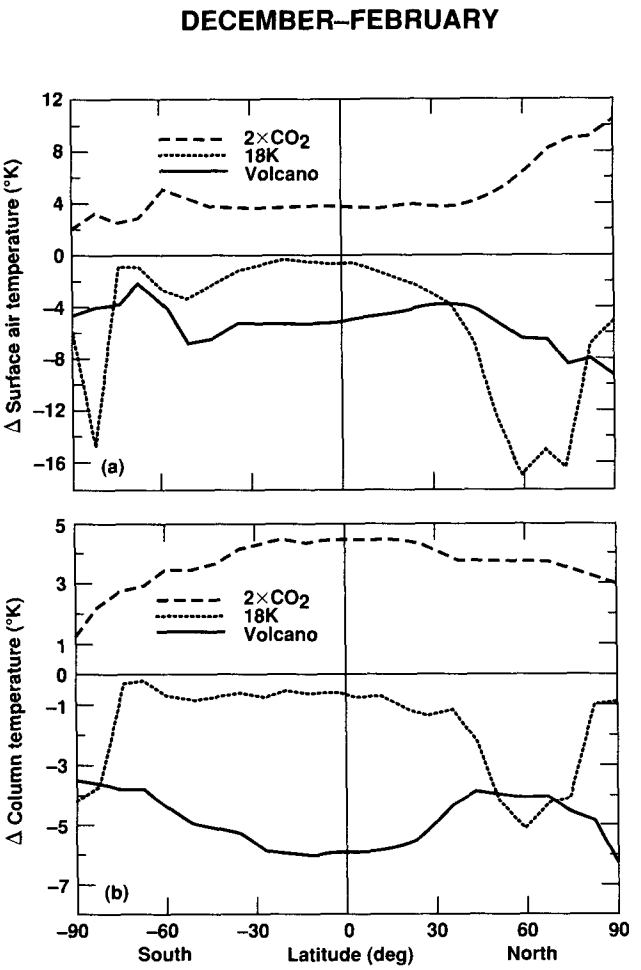

FIG. 10. Change in the zonally and northern winter-(December–February) averaged surface air temperature (a) and vertically integrated air temperature (b) as a function of latitude for the volcano, 2× CO_2, and 18 K runs.

of the winter polar atmosphere limits the amount of heat advected vertically and, hence, the greenhouse warming in the 2× CO_2 experiment tends to be concentrated near the surface there. At low latitudes, the greenhouse warming is distributed throughout much of the troposphere by an enhanced, vigorous penetrative convection (Manabe and Wetherald 1975). Thus, the vertically integrated atmospheric temperature change is actually greatest in the tropics for the 2× CO_2 run (cf. Fig. 10b), since the increase in tropical moisture provides a strong positive feedback at low latitudes. In contrast, there is less of a variation in the vertical distribution of cooling with latitude in the volcano run. For example, penetrative convection in the tropics carries latent heat to lower altitudes for the volcano run than it does for the 2× CO_2 run since there is less moisture close to the surface in the climate-cooling volcano run. Thus, the vertically integrated temperature change

for the volcano run (Fig. 10b) is roughly similar to that at the surface (cf. Fig. 10a). This similarity is also found for the 18 K run, for which the very modest changes in sea surface temperature at low latitudes and the occurrence of elevated ice sheets at northern middle and high latitudes control temperature changes in this run.

Without a major, systematic increase in the latitudinal temperature gradient, the volcano run experiences little change in the eddy kinetic energy in the Northern Hemisphere (cf. Fig. 11a). Also, the longwave energy in the Northern Hemisphere decreases in this experiment (cf. Fig. 11b). By contrast, the 18 K experiment shows a marked enhancement of eddy kinetic energy and longwave energy in the Northern Hemisphere that reflects the marked increase of the latitudinal temperature gradient. The 2× CO_2 run is characterized by a decrease in eddy kinetic energy and shortwave energy, reflecting the decrease in the latitudinal temperature gradient close to the surface.

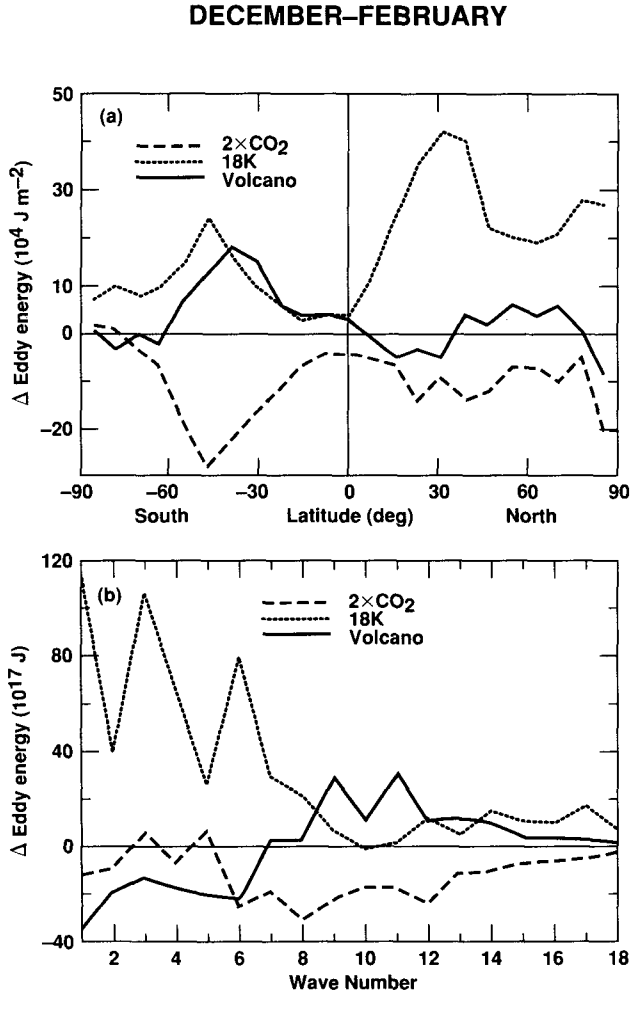

FIG. 11. Changes in zonally and northern winter-averaged eddy kinetic energy for the volcano, 2× CO_2, and 18 K runs. (a) Variation with latitude and (b) variation with wavenumber for the Northern Hemisphere.

As neither the latitudinal temperature gradient nor the eddy kinetic energy show large positive, systematic increases in the Northern Hemisphere for the volcano run, no marked systematic increase occurs in the poleward transport of sensible heat by eddies (cf. Fig. 12a). Once more this behavior for the volcano run is quite different than that for the 18 K run, which does show a large increase in sensible heat transport by eddies in the Northern Hemisphere during winter. Also, this transport is weakened in the 2× CO_2 run.

In both cooling experiments, there is a reduced moisture content at low latitudes, although more so in the volcano run. This change, when combined with an approximately unaltered amount of eddy kinetic energy, results in a marked decrease in the poleward transport of latent heat by eddies in the volcano run (cf. Fig. 12b). (Note that the poleward transport is positive in the north and negative in the south in this figure and in Figs. 12c and 12d.) But in the 18 K run this transport increases slightly due to an enhanced kinetic energy. It also increases in the 2× CO_2 run, due to the enhanced amount of moisture at low latitudes.

The total (sensible plus latent heat) static energy transported poleward by eddies decreases greatly for the volcano run, reflecting the marked decrease in latent heat transport and modest changes in sensible heat transport (cf. Fig. 12c). Also, the total energy transport by eddies and the mean circulation are greatly reduced in this run (cf. Fig. 12d). In contrast, the 2× CO_2 run is characterized by a somewhat weakened eddy transport of sensible heat and a substantial increase in eddy transport of latent heat, which combine to produce a small enhancement of total transport by eddies in the north and a more sizable enhancement of total transport there. Finally, the increased eddy kinetic energy and latitudinal temperature gradient of the ice age run result in a large increase in sensible heat transport by eddies, and overall marked increases in total eddy and total atmospheric transport of static energy.

As can be seen in Fig. 12d, total atmospheric heat transport at low northern latitudes decreases greatly in the volcano run, but not in the other two runs. These changes in transports at low latitudes can be attributed to changes in the Hadley circulation, as driven by latitudinal gradients in latent and sensible heat fluxes from the ocean surface into the atmosphere. In the volcano experiment, the reduced latitudinal gradient in surface temperature at low latitudes implies a reduced gradient in these heat fluxes (e.g., there is a greater reduction in precipitation and, hence, evaporation close to the equator than at somewhat higher latitudes, cf. Fig. 13a). With reduced latent and sensible heat forcing from the tropical oceans, the vertically integrated streamfunction decreases in intensity in the volcano experiment (cf. Fig. 13b; a positive change in the streamfunction in

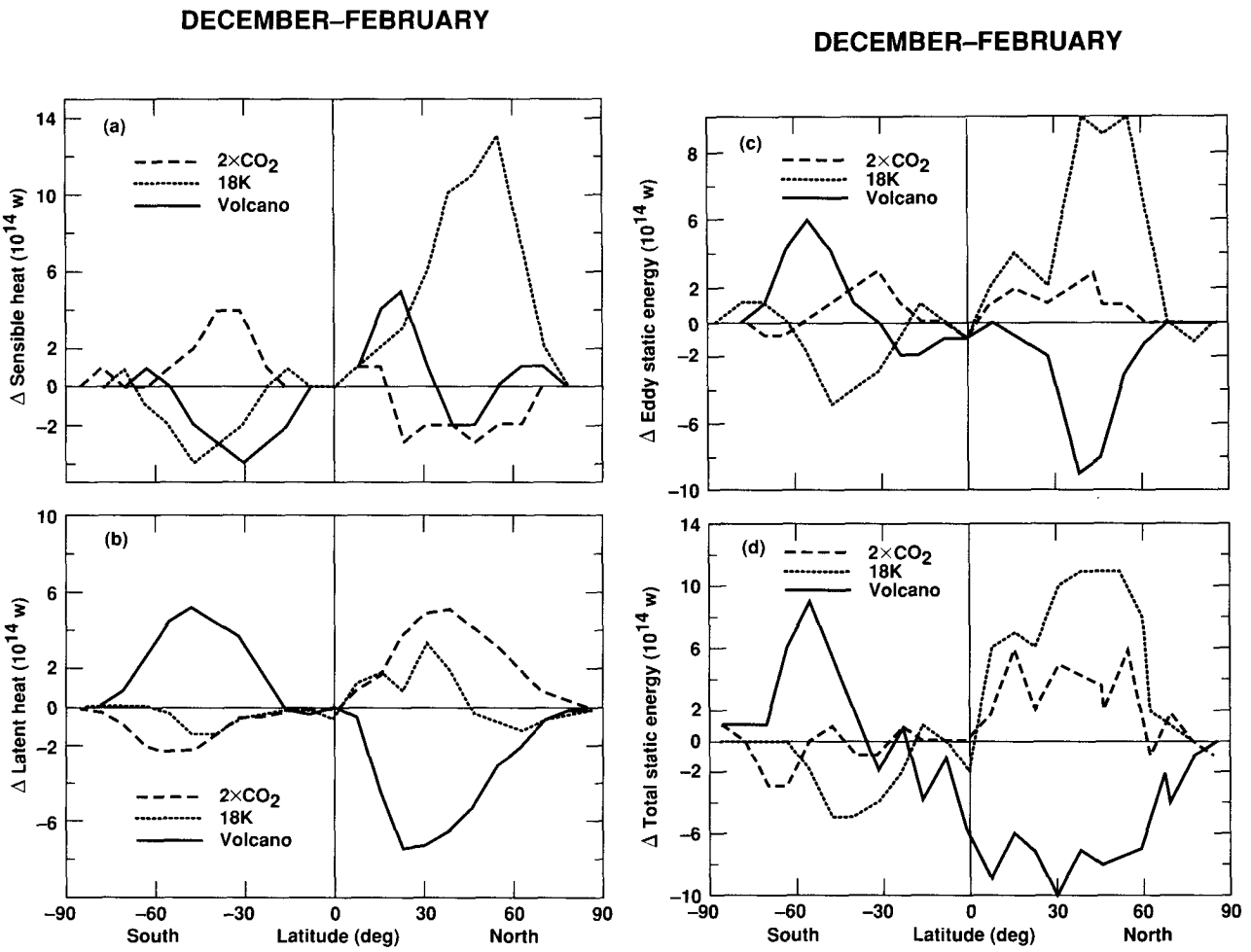

FIG. 12. Changes in zonally and northern winter-averaged heat transport as a function of latitude for the three perturbation runs. (a) Sensible heat transport by eddies; (b) latent heat transport by eddies; (c) sensible plus latent heat transport by eddies; and (d) total heat transport (eddies plus mean circulation). A positive value means transport toward the north.

the Northern Hemisphere indicates a decrease in the Hadley cell intensity). This reduced circulation then transports less energy poleward (cf. Fig. 12d). In a similar vein, the surface temperature gradient at low northern latitudes remains about the same in the 2× CO_2 run and, hence, its Hadley cell intensity remains about the same, while this temperature gradient increases in the 18 K run and, hence, its Hadley cell intensity increases (cf. Figs. 10a and 13b).

Thus, the dynamics in the volcano experiment act to cool high latitudes, rather than warm them, as expected (cf. Fig. 12d). Despite these dynamical tendencies, high latitudes do not cool much more than the tropics in this experiment, perhaps because of the counteracting effects of cloud and dynamical feedbacks. In the 2× CO_2 experiment, the dynamics act as positive feedbacks by trying to warm high latitudes during the winter season. Only in the 18 K experiment does the dynamics act in the expected way by exerting a negative feedback on cooling at high latitudes. But, this case shows the largest absolute values for ΔT_s at high northern latitudes during winter (Fig. 10a). Thus, the warm and cold experiments are not mirror images of one another nor do the two cold experiments show the same behavior. Models (e.g., energy balance models) that operate on the assumptions noted at the beginning of this subsection would not reproduce the results of the GCM runs considered here. Furthermore, as illustrated particularly by the results from the volcano run, there is not a simple relationship between the change in the eddy transports and the change in the local latitudinal temperature gradient (cf. Figs. 10a, 12a).

The above discussion of the dynamical changes in the three climate experiments provides a context for interpreting the changes in cloudiness exhibited by them (cf. Fig. 6a). At middle latitudes, variations in baroclinicity (or storminess), as measured by changes in eddy energy (cf. Fig. 11a), can play a major role in

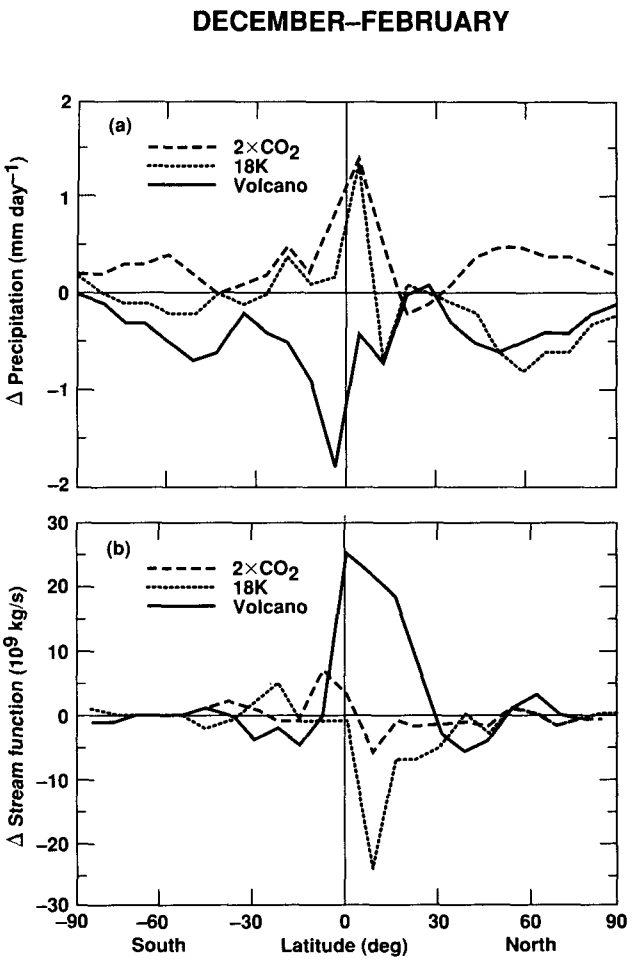

FIG. 13. Changes in zonally and northern winter-averaged (a) precipitation and (b) vertically integrated mass streamfunction for the three perturbation cases. An enhanced, thermally direct mean meridional circulation corresponds to negative changes in the streamfunction in the Northern Hemisphere and positive ones in the Southern Hemisphere.

causing changes in cloud fraction, while at low latitudes changes in the intensity of the Hadley circulation (cf. Fig. 13b) can be important. In the Southern Hemisphere, the eddy energy increases significantly at midlatitudes for the volcano and 18 K runs, thereby enhancing the fractional cloudiness at these latitudes, while just the opposite occurs for the 2× CO_2 run. Also, an enhanced moisture convergence occurs at these latitudes in the volcano run, while an enhanced moisture divergence occurs there in the 2× CO_2 run (cf. Fig. 12b). These changes in moisture transport also favor the computed changes in cloudiness. Finally, there is little change in the intensity of the Hadley circulation in the Southern Hemisphere for any of the runs (cf. Fig. 13b) so that it is not an important factor in the cloud changes under consideration.

A distinctly different set of changes occurs in the Northern Hemisphere. The eddy energy increases greatly at midlatitudes for the 18 K run, changes little for the volcano run, and undergoes a modest decrease for the 2× CO_2 run. Also, the Hadley circulation greatly increases for the 18 K run, varies little for the 2× CO_2 run, and decreases significantly for the volcano run. The changes in cloudiness at northern midlatitudes for the 18 K and 2× CO_2 runs can be attributed to the above-cited changes in eddy energy. The small increase in cloudiness near 30° latitude in the volcano run is caused by the weakening of the Hadley circulation, which shifts the latitude band of its subsidence equatorward, that is, there is reduced subsidence where there is enhanced cloudiness. Also, there is an enhanced moisture convergence in the volcano run at latitudes below about 30°.

The above discussion illustrates that there need not be mirror symmetry between changes in climate variables between cooling and warming forcings, nor symmetry in the changes that occur in the two hemispheres. From a dynamical perspective, differences in latitudinal surface temperature gradients play a key role in causing this breakdown in symmetry. From a somewhat broader perspective, we can attribute the breakdown in cooling/warming symmetry to asymmetries in the primary radiative forcing. In particular, the radiative forcing in the volcano run is approximately twice as strong at the equator as it is at the poles (cf. Fig. 8a); it is nearly independent of latitude in the 2× CO_2 run (cf. Fig. 8b); and it is strongly concentrated at high latitudes in the 18 K run. We attribute the breakdown in hemispherical symmetry to the asymmetry in the distribution of landmasses and oceans. This basic asymmetry is reflected in the GCM runs in terms of asymmetries in such climate variables as the amount of sea ice. Changes in these variables in turn produce changes in latitudinal temperature gradients and, hence, eddy energies.

The above basic causes of cooling/warming and hemispherical asymmetries provide a starting point for understanding the fundamental reasons for the major differences in the latitudinal profiles of ΔT_s exhibited by the three climate experiments (cf. Figs. 3a and 10a). In a gross sense, this profile is flattest for the volcano experiment; it is steeper for the 2× CO_2 run (i.e., ΔT_s increases toward higher latitudes); and it is steepest for the 18 K experiment. These differences are direct reflections of the above-cited differences in the latitudinal distribution of the primary radiative forcing. In all three cases, large changes in sea ice at high southern latitudes significantly enhance ΔT_s at these locations (cf. Fig. 3a). Consequently, these changes represent a major mechanism for creating hemispherical asymmetries.

Radiative and dynamical responses to the primary radiative forcing have a major impact on the fine structure of the ΔT_s profiles. These responses produce changes in latitudinal heat transport, cloudiness, and water vapor abundances. They also involve different

components of the circulation at low (Hadley) and high latitudes (eddy). For example, a less vigorous Hadley circulation in the Northern Hemisphere for the volcano run (cf. Fig. 13b) plays an important role in creating a ΔT_s profile that decreases from the equator to midlatitudes in the Northern Hemisphere. The altered Hadley circulation leads to sharply varying perturbations in advective heat flux, cloud fraction, and water vapor with latitude at low northern latitudes (cf. Fig. 8a) that jointly help to create, in a self-consistent/interactive manner, the net ΔT_s profile. By way of contrast, the Hadley circulation in the Northern Hemisphere is less perturbed in the $2\times CO_2$ experiment and the various feedback factors show less steep variations at low northern latitudes for this run than they do for the volcano run (cf. Figs. 8a and 8b).

4. Discussion and summary

Volcanic particles in the stratosphere due to a single volcanic event typically have lifetimes on the order of one to several years (e.g., Toon and Pollack 1982; McCormick et al. 1984). This time scale is longer than the radiative response time of the lower stratosphere, but is much shorter than the response time of the coupled troposphere/ocean system. When just the heat capacity of the upper mixed layer is considered, the *e*-folding time scale for cooling by steady-state volcanic forcing is approximately 15 years (cf. Fig. 1a). When allowance is made for heat exchange between the mixed layer and the deeper portions of the ocean based on observations of passive tracers this time scale increases by as much as a factor of 10 (paper 2). Also, according to the GFDL coupled atmosphere/ocean GCMs, southern high latitudes may respond much more slowly than other latitudes to climate forcings because of very deep mixing that occurs in and adjacent to the Antarctic circumpolar ocean (Stouffer et al. 1989; Manabe et al. 1991). Thus, a single volcanic cloud can drive temperatures in the lower stratosphere to essentially their steady-state values. But, temperature changes in the troposphere are only a small fraction of their steady-state values, in accordance with 1D radiative convective simulations of the Mt. Agung and the El Chichón volcanic clouds (Hansen et al. 1980; Pollack and Ackerman 1983) and GCM simulations of the Mt. Pinatubo cloud (Hansen et al. 1992).

Closely spaced, multiple, sulfur-rich, volcanic explosions are required to produce large increases in stratospheric aerosols over time scales comparable to the response time of the troposphere/ocean system (decades–centuries). As illustrated by the calculations reported here, large changes in globally averaged surface temperature can occur when this condition is met and when the globally and time-averaged optical depth of the volcanic particles is on the order of 0.1. Due to possible linkages between plate tectonics and volcanic explosions, such epochs of multiple volcanic explosions may occur from time to time, as exemplified by the 30-year period at the end of the nineteenth and beginning of the twentieth centuries when a sustained, significant optical depth perturbation by volcanic particles occurred (Pollack et al. 1976b). Such epochs introduce a level of uncertainty in predicting the future course of the earth's climate, due to the steadily increasing amounts of greenhouse gases in the earth's atmosphere.

The earth's climate is modified in a number of major ways by sustained volcanic forcing with a time- and space-independent optical depth of 0.15, according to GISS climate model II. The annually averaged amount of sea ice expands by more than a factor of 2, chiefly at high southern latitudes. This prediction is consistent with a comparable expansion of sea ice that characterized the climate at the height of the last ice age, which had a globally averaged decrease in surface temperature comparable to that in the volcano run (CLIMAP 1981). However, the variation of ΔT_s with latitude for the volcano and 18 K simulations are quite different. The absolute magnitude of ΔT_s increases strongly from low to high latitude in the 18 K run, but shows a much flatter profile for the volcano run. This difference is due in part to the occurrence of elevated ice sheets at middle to high northern latitudes in the 18 K run. For similar reasons, the surface albedo of the volcano run shows its largest variation at high southern latitudes, where most of the change in sea ice occurs, while the 18 K run exhibits both this change in surface albedo and one of comparable amplitude and greater extent at middle to high northern latitudes, where land ice is present.

Differences in sea ice changes between the 18 K and volcano runs may well reflect limitations of both the CLIMAP data and the GISS climate model II. In particular, sea ice may have increased somewhat less (by 10% to 20%) than is indicated by the CLIMAP reconstruction of the peak of the last ice age (see paper 2). The GISS climate model II has a simplistic sea ice scheme, one which probably overestimates the sea ice response, especially for short time scale changes (i.e., changes that occur faster than the time in which North Atlantic Deep Water changes). Furthermore, in the volcano experiment the GISS model did not take account of changes in ocean circulation, which could impact the extent of sea ice. It seems highly likely that changes in ocean circulation affected the extent of sea ice at the peak of the last glaciation. However, such circulation changes would have had far less time to develop in the shorter time scale volcano run. In summary, differences in the changes in sea ice distribution between the two experiments are definitely suspect. The CLIMAP data may also have problems with temperatures at low latitudes (paper 2). In reality, they may have been a bit colder (by 1 to 2 K). None of the conclusions of the last paragraph or the rest of the paper would be modified in a significant way if plausible al-

ternative sea ice distributions and low-latitude temperatures were incorporated into the 18 K simulation.

The above differences in the volcano and 18 K runs reflect their most fundamental difference. The volcano run is relevant to the response of the climate system to a sustained radiative cooling over time scales of centuries, long enough for changes of temperature in the upper levels of the ocean to reach steady-state values and long enough for short time scale feedbacks, such as water vapor, albedo, clouds, and atmospheric dynamics to be fully effective. The 18 K run simulates a climate state in which longer time scale changes have occurred. These include the emplacement of extensive ice sheets on the North American and Eurasian landmasses, a reduction in the mixing ratios of CO_2 and other greenhouse gases, and changes in the spatial distribution of vegetation.

Given the above differences between the 18 K and volcano runs, it is perhaps not surprising that their climatologies differ in some important ways. In this regard, it is interesting to compare the similarities and differences between the volcano and 2× CO_2 runs. In both cases, radiative drives act as the primary forcing mechanism for climate change and the steady-state response of the climate system for time scales of centuries was determined. The two cases differ in that cooling occurred in the volcano run and warming occurred in the 2× CO_2 run and in that the volcanic particles were most effective in the solar part of the spectrum, whereas CO_2 affected almost solely the thermal portion of the spectrum.

In certain ways, the results of the volcano and 2× CO_2 runs are quite similar to one another. The fraction of the total globally averaged surface temperature change due to direct radiative forcing was quite similar: 25% for the 2× CO_2 run versus 30% for the volcano run. In both cases, changes in water vapor constituted the most important feedback mechanism, with it accounting for about 45% of the total globally averaged change in surface temperature. At high latitudes, changes in surface albedo, due primarily to changes in the spatial extent of sea ice, produced a large positive feedback effect. Finally, in both cases, the cloud and advective heat transport feedbacks had a strong tendency to have opposite signs at a given latitude, so that their combined effect was relatively weak.

Despite the above similarities between the climate changes occurring in the volcano and 2× CO_2 runs, there were some important differences. The latitudinal profiles of the change in surface air temperature, ΔT_s, were different in the two runs, especially at low and midlatitudes of the Northern Hemisphere (Figs. 3a and 10a). This difference and the implied difference in the latitudinal variation of atmospheric temperature aloft are, in part, responsible for significant differences in the dynamical changes that occurred in the two runs. Changes in heat transported by eddies, heat transported by the total circulation, the strength of the Hadley circulation, eddy energy, and eddy wavenumber spectrum in the volcano and 2× CO_2 runs are far from being mirror images of one another (cf. Figs. 11–13).

There are also other aspects of the volcano and 2× CO_2 runs that indicate that they are not mirror images of one another. The volcano run takes almost twice as long to reach a steady-state climate due to a combination of the low thermal inertia of sea ice and the T^{-3} dependence of the radiative time constant (cf. Figs. 1a and 1b). The increase in sea ice in the volcano run is much larger than the decrease in sea ice in the 2× CO_2 run; that is, the ice albedo feedback is stronger when the climate cools than when the climate warms. The ΔT_s associated with the direct radiative forcing by volcanic particles shows a much stronger variation with latitude than that occurring in the 2× CO_2 run (cf. Figs. 8a and 8b), reflecting important differences (cited above) in the nature of the two radiative forcings. This difference in primary radiative forcing, as well as that for the 18 K run (as expressed by ΔA_s), engenders radiative and dynamical feedbacks with differing latitudinal profiles, resulting in net ΔT_s profiles that differ considerably. Thus, although there are important asymmetries in the response of the climate system to warming versus cooling climate change agents, as cited above, what matters the most is the latitudinal profile of the primary radiative forcing.

All the above differences among the three climate perturbation experiments suggest that it is difficult to arrive at simple prescriptions for key climate processes to be used in energy balance climate models. Specifically, there does not seem to be an obvious relationship between the magnitude of the globally averaged change in surface temperature and the changes in advective heat transport and properties of key dynamical components (cf. Figs. 11–13).

One could imagine a more sophisticated type of energy balance model for which there are temperature-dependent mechanisms (e.g., transport of latent heat) in addition to diffusive mechanisms. It will be an extreme challenge, however, to devise such a parameterization, for two reasons. First, as illustrated in Fig. 9, the water vapor feedback is not simply due to a change in the column abundance of water vapor resulting from a modified surface temperature. Rather, several dynamical processes also influence the total water vapor feedback. Their latitudinal dependencies are both complicated and significantly varied among the three types of climate changes considered. Second, even the column component of the water vapor feedback depends on the net ΔT_s due to all processes, which is the quantity that the energy balance model is trying to determine, as opposed to knowing it in advance. Nevertheless, the results of this paper may offer some useful constraints for developing improved energy balance models and the authors of this paper will be glad to provide more detailed information to those interested in pursuing this course.

5. Conclusions

Perhaps the largest surprise to come from our analyses of the steady-state climate responses to three different forcings is the obvious presence of asymmetries of several types. The climate response to a warm forcing, as exemplified by $2\times CO_2$, and that to a cold forcing, as exemplified by volcanic particles, are not mirror images of one another. Similarly, there are important differences in the climate response to two different cold forcings—volcanic particles and ice age—and there are important differences in the responses in the Southern and Northern hemispheres. The sources of these asymmetries include differences in the latitudinal dependence of the primary radiative forcings, differences in the amount of land and ocean in the two hemispheres, the much greater expansion of sea ice for cold forcings than for warm forcings, the nonlinear dependence of the strength of turbulent mixing on the sign of the temperature stratification, and the obviously important impact that extensive land ice sheets have on the 18 K simulations.

The GISS climate model II provides a reasonable representation of the earth's current climate and, in this sense, it is an appropriate model to use for examining climate changes, both past and future. However, like essentially all other current GCM climate models, it has a number of important limitations. These include a crude parameterization of cloud feedbacks that does not allow for changes in the radiative properties of clouds, an overly simplified scheme for determining when and where sea ice occurs, and, of course, the lack of a coupled ocean GCM to define ocean heat transport feedbacks. Nevertheless, we suspect that many of the qualitative aspects of our calculations, including the climate asymmetries, are robust features that will be present when more sophisticated climate models are applied to the problems considered here.

General circulation climate models, including the GISS model, will continue to evolve by adding better and more complete physics. But, it is essential that they be subjected to thorough validation through comparisons with relevant observations. There has been a tendency to "tune" GCMs to agree with the basic properties of the earth's current climate. To this degree, they are vehicles of questionable validity when applied to climate change problems. Spacecraft data are beginning to provide the type of information that is needed to subject climate models to serious and meaningful tests. Examples of this type of observational data were given in the discussion of the water vapor and cloud feedbacks. More generally, it will be important to devise ways of determining observationally the key climate feedbacks over a wide range of latitudes for comparison with the predictions of climate models. A major step forward in this regard will take place when the next generation of spacecraft are deployed (e.g., NASA's EOS spacecraft). Airborne and ground-based platforms can also play a role here by providing essential data that constrains the nature of key subgrid-scale processes (e.g., those involving clouds).

The El Chichón and Mount Pinatubo volcanic clouds offer important opportunities for gaining an improved understanding of climate changes through observation and for testing the ability of climate models to predict the temporal response of the climate system to large amplitude but transient forcings. Such opportunities exist because both the forcing and the response are well characterized through a combination of satellite, airborne, and ground-based observations.

Acknowledgments. This research was supported by grants from NASA's Earth System Science Modeling Program Office. We are grateful to John Mitchell for his insightful review of this paper, which lead to significant improvements in it.

REFERENCES

Broccoli, A. J., and S. Manabe, 1987: The influence of continental ice, atmospheric CO_2, and land albedo on the climate of the last glacial maximum. *Climate Dyn.*, **1**, 87–99.

Cess, R. D. et al., 1989: Interpretation of cloud-climate feedback as produced by 14 atmospheric general circulation models. *Science*, **245**, 513–516.

——, 1990: Intercomparison and interpretation of climate feedback processes in 19 atmospheric general circulation models. *J. Geophys. Res.*, **95**, 16 601–16 615.

CLIMAP Project, 1981: *Seasonal Reconstruction of the Earth's Surface at the Last Glacial Maximum.* Geol. Soc. Amer., Map and Chart Series, No. 36.

Denton, G. H., and T. J. Hughes, 1981: *The Last Great Ice Sheets.* John Wiley, 484 pp.

Deshler, T., D. J. Hofmann, B. J. Johnson, and W. R. Rozier, 1992: Balloonborne measurements of the Pinatubo aerosol size distribution and volatility at Laramie, Wyoming during the summer of 1991. *Geophys. Res. Lett.*, **19**, 199–202.

Fu, R., A. D. Del Genio, W. B. Rossow, and W. T. Liu, 1992: Cirrus-cloud thermostat for tropical sea surface temperatures tested using satellite data. *Nature*, **358**, 394–397.

Gordon, A. L., 1982: *Southern Ocean Atlas.* Columbia University Press, 84 pp.

Hansen, J. E., and J. B. Pollack, 1970: Near-infrared light scattering by terrestrial clouds. *J. Atmos. Sci.*, **27**, 265–281.

——, and A. A. Lacis, 1990: Sun and dust vs. the greenhouse. *Nature*, **346**, 713–719.

——, ——, P. Lee, and W. C. Wang, 1980: Climatic effects of atmospheric aerosols. *Ann. New York Acad. Sci.*, **338**, 575–587.

——, G. Russell, D. Rind, P. Stone, A. Lacis, S. Lebedeff, R. Ruedy, and L. Travis, 1983: Efficient three-dimensional global models for climate studies: Models I and II. *Mon. Wea. Rev.*, **111**, 609–662.

——, A. Lacis, D. Rind, G. Russell, P. Stone, I. Fung, R. Ruedy, and J. Lerner, 1984: Climate sensitivity: Analysis of feedback mechanisms. *Climate Processes and Climate Sensitivity, Geophys. Monogr. 29*, Maurice Ewing Vol. 5, Amer. Geophys. Union, 130–163.

——, J. B. Pollack, R. Ruedy, and M. Sato, 1992: Potential climate impact of Mount Pinatubo eruption. *Geophys. Res. Lett.*, **19**, 215–218.

Harshvardhan, A., Arking, M. D. King, and M-D Chou, 1984: Impact of the El Chichón stratospheric aerosol layer on Northern Hemisphere temperatures. *Aerosols and Their Climatic Effects*, Deepak, 261–273.

Hofmann, D. J., and J. M. Rosen, 1983: Stratospheric sulfuric acid

fraction and mass estimate for the 1982 volcanic eruption of El Chichon. *Geophys. Res. Lett.*, **10,** 313–316.

Labitzke, K., B. Naujokat, and M. P. McCormick, 1983: Temperature effects on the stratosphere of the April 4, 1982 eruption of El Chichon, Mexico. *Geophys. Res. Lett.*, **10,** 24–26.

Lacis, A. A. and J. E. Hansen, 1974: A parameterization for the absorption of solar radiation in the earth's atmosphere. *J. Atmos. Sci.*, **31,** 118–133.

——, and V. Oinas, 1991: A description of the correlated *k* distribution method for modeling nongrey absorption, thermal radiation, and multiple scattering in vertically inhomogeneous atmospheres. *J. Geophys. Res.*, **96,** 9027–9063.

Lindzen, R. S., 1990: Some coolness concerning global warming. *Bull. Amer. Meteor. Soc.*, **71,** 288–299.

McCormick, M. P., T. J. Swissler, W. H. Fuller, W. H. Hunt, and M. T. Osborn, 1984: Aircraft and ground-based lidar measurements of the El Chichon stratospheric aerosol from 90 N to 56 S. *Geof. Int.*, **23-2,** 187–221.

Manabe, S., and R. T. Wetherald, 1967: Thermal equilibrium of the atmosphere with a given distribution of relative humidity. *J. Atmos. Sci.*, **24,** 241–259.

——, and ——, 1975: The effects of doubling the CO_2 concentration on the climate of a general circulation model. *J. Atmos. Sci.*, **32,** 3–15.

——, R. J. Stouffer, M. J. Spelman, and K. Bryan, 1991: Transient responses of a coupled ocean–atmosphere model to gradual changes of atmospheric CO_2. Part I: Annual mean response. *J. Climate*, **4,** 785–818.

NOAA, 1974: *User's Guide to NODC Data Services.* Environmental Data Services, NODC.

Oberbeck, V. R., E. F. Danielsen, K. G. Snetsinger, and G. V. Ferry, 1983: Effect of the eruption of El Chichón on stratospheric aerosol size and composition. *Geophys. Res. Lett.*, **10,** 1021–1024.

Palmer, K. F., and D. Williams, 1975: Optical constants of sulfuric acid: Application to the clouds of Venus? *J. Opt. Soc. Amer.*, **14,** 208–219.

Pollack, J. B., and T. P. Ackerman, 1983: Possible effects of the El Chichón volcanic cloud on the radiation budget of the northern tropics. *Geophys. Res. Lett.*, **10,** 1057–1060.

——, and C. P. McKay, 1985: The impact of polar stratospheric clouds on the heating rates of the winter polar stratosphere. *J. Atmos. Sci.*, **42,** 245–262.

——, F. C. Witteborn, K. O'Brien, and B. Flynn, 1991: A determination of the infrared optical depth of the El Chichón volcanic cloud. *J. Geophys. Res.*, **96,** 3115–3122.

——, O. B. Toon, E. F. Danielsen, D. J. Hofmann, and J. M. Rosen, 1983: The El Chichon volcanic cloud: An introduction. *Geophys. Res. Lett.*, **10,** 989–992.

——, ——, C. Sagan, A. Summers, B. Baldwin, and W. Van Camp, 1976a: Volcanic explosions and climatic change: A theoretical assessment. *J. Geophys. Res.*, **81,** 1071–1083.

——, ——, A. Summers, B. Baldwin, C. Sagan, and W. Van Camp, 1976b: Stratospheric aerosols and climatic change. *Nature*, **263,** 551–555.

Ramanathan, V., and W. Collins, 1991: Thermodynamic regulation of ocean warming by cirrus clouds deduced from observations of the 1987 El Nino. *Nature*, **351,** 27–32.

Raval, A., and V. Ramanathan, 1989: Observational determination of the greenhouse effect. *Science*, **342,** 758–761.

Rind, D., and B. Peteet, 1985: Terrestrial conditions at the last glacial maximum and CLIMAP sea surface temperature estimates: Are they consistent? *Quat. Res.*, **24,** 1–22.

——, N. K. Balachandran, and R. Suozzo, 1992: Climate change and the middle atmosphere. Part II: The impact of volcanic aerosols. *J. Climate*, **5,** 189–208.

——, R. Suozzo, N. K. Balachandran, and G. Russell, 1988: The GISS global climate/middle stratosphere model. Part I: Model structure and climatology. *J. Atmos. Sci.*, **45,** 329–370.

——, E.-W. Chiou, W. Chu, J. Larsen, S. Oltmans, J. Lerner, M. P. McCormick, and L. McMaster, 1991: Positive water vapor feedback in climate models confirmed by satellite data. *Nature*, **349,** 500–503.

Stouffer, R. J., S. Manabe, and K. Bryan, 1989: Interhemispheric asymmetry in climate response to a gradual increase in atmospheric CO_2. *Nature*, **342,** 660–662.

Toon, O. B., and J. B. Pollack, 1976: A global average model of atmospheric aerosols for radiative transfer calculations. *J. Appl. Meteor.*, **15,** 225–246.

——, ——, 1982: Stratospheric aerosols and climate. *The Stratospheric Aerosol Layer,* R. C. Whitten, Ed., Springer-Verlag, 121–148.

Valero, F. P. J., and P. Pilewskie, 1992: Latitudinal survey of spectral optical depths of the Pinatubo volcanic cloud-derived particle sizes, columnar mass loadings, and effects on planetary albedo. *Geophys. Res. Lett.*, **19,** 163–166.

Wetherald, R. T., and S. Manabe, 1988: Cloud feedback processes in a general circulation model. *J. Atmos. Sci.*, **45,** 1397–1415.